# Conceptualization and Multi-Objective Optimization of the Electric System of an Airborne Wind Turbine

J. W. Kolar
T. Friedli
F. Krismer
A. Looser
M. Schweizer
P. Steimer
J. Bevirt

Eidgenössische Technische Hochschule Zürich
Swiss Federal Institute of Technology Zurich

# Conceptualization and Multi-Objective Optimization of the Electric System of an Airborne Wind Turbine

J. W. Kolar, T. Friedli, F. Krismer, A. Looser, M. Schweizer
Power Electronic Systems Laboratory (PES)
ETH Zurich, 8092 Zurich, Switzerland
kolar@lem.ee.ethz.ch

P. Steimer
ABB Switzerland Ltd.
5300 Turgi, Switzerland
peter.steimer@ch.abb.com

J. Bevirt
Joby Energy, Inc.
Santa Cruz, CA 95060
info@jobyenergy.com

*Abstract*—**Airborne Wind Turbines (AWT) represent a radically new and fascinating concept for future harnessing of wind power. This concept consists of realizing only the blades of a conventional wind turbine (CWT) in the form of a power kite flying at high speed perpendicular to the wind. On the kite are mounted a turbine, an electrical generator and a power electronics converter. The electric power generated is transmitted via a medium voltage cable to the ground. Because of the high flight speed of the power kite, several times the actual wind speed, only a very small swept area of the turbine is required according to Betz's Law and/or a turbine of low weight for the generation of a given electric power. Moreover, because of the high turbine rotational speed, no gear transmission is necessary and the size of the generator is also reduced. For takeoff and landing of the power kite, the turbines act as propellers and the generators as motors, i.e. electric power is supplied so that the system can be maneuvered like a helicopter. In the present work the configuration of power electronics converters for the implementation of a 100 kW AWT is considered. The major aspect here is the trade-off between power-to-weight ratio (W/kg) and efficiency. The dependence of cable weight and cable losses on the voltage level of power transmission is investigated, and a comparison made of low voltage (LV) and medium voltage (MV) versions of generators. Furthermore, the interdependence of the weight and efficiency of a bidirectional Dual Active Bridge dc–dc converter for coupling the rectified output voltage of a LV generator to the MV cable is discussed. Based on this, the concept offering the best possible compromise of weight and efficiency in the power electronics system is selected and a model of the control behavior is derived for both power flow directions. A control structure is then proposed and dimensioned. Furthermore, questions of electromagnetic compatibility and electrical safety are treated. In conclusion, the essential results of the work are summarized and an outlook on future research is given. To enable the reader to make simplified calculations and a comparison of a CWT with an AWT, the aerodynamic fundamentals of both systems are summarized in highly simplified form in an Appendix, and numerical values are given for the 100 kW system discussed in this work.**

*Index Terms*—**airborne wind turbine, multi-objective optimization, power electronics, wind power, renewable energy.**

## I. INTRODUCTION

Wind power and solar thermal energy are currently the economically most viable forms of renewable energy. For the conversion of the kinetic energy of wind into electrical energy, ground-based windmills with horizontal axis are generally employed. The generator, driven by the rotor blades via a gearbox, and the connected power electronics converter for coupling to the grid are housed in a nacelle at the top of a tower. The tower height is dimensioned according to the length of the rotor blades and/or the power of the windmill since according to Betz [1], the maximum power that can be extracted from the wind is given by

$$P_{\text{T,i}} = \frac{8}{27} \rho A_{\text{T}} v_{\text{W}}^3 \qquad (1)$$

(cf. Appendix A1), where $A_{\text{T}}$ is the area swept by the rotor blades, $\rho$ the density of air, and $v_{\text{W}}$ the wind speed. Windmills of high power hence require high towers and overall a very large fraction of mechanically supporting parts at high cost. For example, even a
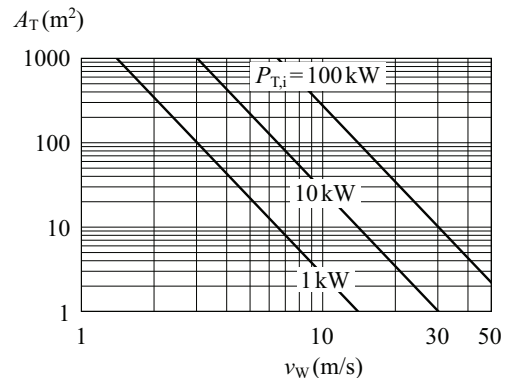


Fig. 1. Dependency of the maximum output power $P_{\text{T,i}}$ of a wind turbine on the area $A_{\text{T}}$ swept by the rotor blades and the wind speed $v_{\text{W}}$ (cf. (1) and (65), parameter $c_{\text{P}} = c_{\text{P,i}} = 0.59$).

very small windmill with 100 kW output already involves an overall weight of the tower of 18 t, whereby the weight of the nacelle is an additional 4.4 t and that of the rotor blades 2.3 t (3-blade rotor, $\omega_{\text{T}} = 47$ rpm, dimensioned for $v_{\text{W}} = 13$ m/s). This fundamental limitation of conventional wind turbines and the lower ground friction and hence increasing wind speed $v_{\text{W}}$ and constancy with increasing altitude $h$ given by

$$v_{\text{W}}(h) = v_{\text{W}}^* \left( \frac{h}{h^*} \right)^{\alpha_{\text{H}}} \qquad (2)$$

($h^*$ and $v_{\text{W}}^*$ are a reference height and speed, and $\alpha_{\text{H}} = 0.1 \ldots 0.6$ is the Hellmann's exponential, depending on the ground surface and vertical temperature gradients) have led to the suggestion of radically new concepts for wind energy exploitation, based on initial considerations by Loyd [2]. The basic idea here consists of implementing only the blades of the windmill in the form of a power kite flying at high speed perpendicular to the wind, thus avoiding the entire mechanical support structure of conventional windmills. The ideas go as far as exploitation of the wind energy in the jetstream at an altitude of $10'000$ m with wind speeds of up to $50$ m/s (compared to typically $10$ m/s near the ground) and/or a 125-fold higher power density (W/m²) according to (1) compared for example to $v_{\text{W}} = 10$ m/s. However, also an increase in $v_{\text{W}}$ by only 25% already results in a doubling of the power density (cf. Fig. 1). Now the technical challenge of this fascinating concept consists in transmitting the wind power to the ground. For this purpose two possible methods are discussed: on the one hand, the power absorbed by the power kite could be converted via a tether into torque on a tether drum situated on the ground, which drives a generator. To suppress twisting in the

Fig. 2. Demonstrator of an Airborne Wind Turbine (AWT) system of Joby Energy [9].
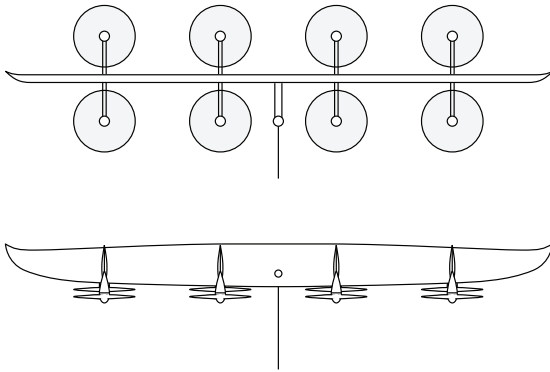


Fig. 3. Conceptual drawing of aerofoil and turbines of a 100 kW AWT system of Joby Energy [9]; length / width: 11 m / 1 m.
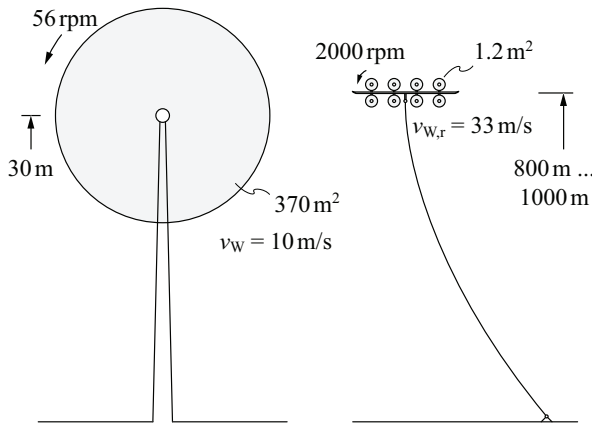


Fig. 4. Comparison of the physical size of a conventional ground-based 100 kW wind turbine and an AWT of equal power output. For the calculation of the given numerical values please see Appendix A5.

tether, the power kite is flown in a figure-of-eight trajectory and the tether is unrolled by the pull of the kite; in a recovery phase the kite is subsequently turned out of the wind, lowering the force acting upon it, and the tether rolled up again. The cycle is then periodically repeated. The versions of this concept, generally known as a pumping power kite, range from direct conversion (SwissKitePower, [3]) to carousel-like structures with several kites (KiteGen, Univ. of Torino, [4], [5]) and Laddermill structures [6], whereby a significant challenge is caused not only by the construction, but also by the optimal flight control of the kite to assure maximum power gain [7], [8].
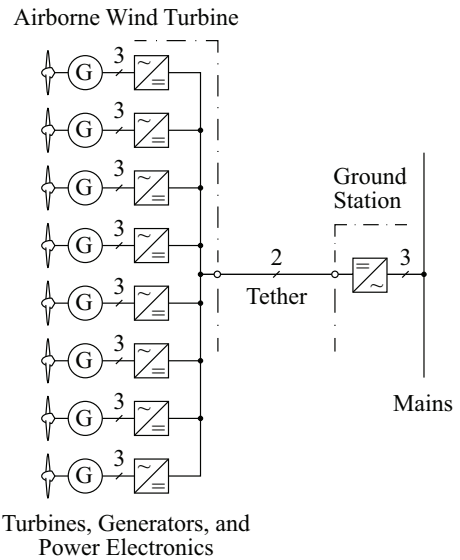


Fig. 5. AWT basic electric system structure.

Alternatively, the power kite may be equipped with a turbine and an electric generator, together with a power electronics converter, and the power is transmitted electrically to the ground (cf. Fig. 2 and Fig. 3). Since the power kite flies at very high speed perpendicular to the wind, i.e. at several times the actual wind speed, only a very small turbine area is required according to (1) or a turbine of low weight for the generation of a given electric power, compared with ground-based systems (cf. Fig. 1 and Fig. 4). Moreover, because of the high turbine speed, no gear transmission is necessary and the size of the generator is also reduced.

For takeoff and landing of the power kite, the turbines act as propellers and the generators as motors, i.e. electric power is supplied so that the system can be maneuvered like a helicopter. In general, flight trajectory control is here also one of the challenges, whereby it must be said that compared to a pumping power kite, where only mechanical control is possible, a more direct control influence is available via the generators/motors. This concept, generally known as Airborne Wind Turbines (AWT), is being pursued by several innovative companies such as Sky WindPower [10], and Joby Energy [9] / Makani Power [11], partly supported by the US Department of Energy (DoE) and Google.

Investigations and demonstrations of AWT to date have been mainly limited to the aerodynamic part, i.e. to the aerofoils, as well as the generators, the connected rectifier/inverter and the cable for energy transmission (tether) to the ground. This motivates an overall analysis of the electrical and power electronics systems required for the implementation of an AWT (cf. Fig. 5) in the present work, which also includes the control aspect. Here the main question, apart from the structure of the power electronics system, is the voltage level of the power transmission to the ground and in general the trade-off between power-to-weight ratio (W/kg) (additional explanation cf. A6) and efficiency of the individual converter stages, since the weight of the electrical system, including the transmission cable, must be supported by the power kite. On the basis of this analysis, favorable parameters can be determined and the technical feasibility assured. A further motivation is the multi-disciplinary character of the subject, which is of increasing importance for power electronics research at universities. Furthermore, there exist close couplings of this subject

to current questions in the area of More Electric Aircraft [12] and Smart Grids [13] – the power electronics system of the AWT can be regarded as a Smart Pico Grid – or in general to the multi-objective optimization of converter systems [14], [15].

The analysis is conducted with the example of a demonstrator system of Joby Energy with 8 turbines on an aerofoil made of composite material with an overall power of the turbines (shaft) of $100\,kW$. The system is designed to fly at $800 \ldots 1000\,m$. To reduce the complexity, the system is initially not considered as a whole, but divided up into main functional elements, which are analyzed separately; the results are then consolidated.

In an initial step (Section II-A), possible configurations of power electronics converters are considered for the conversion and collection of the electric power accruing with variable rpm at the output of the generators for transmission via a MV cable to the ground station. Based thereupon, 2 main concepts are selected for more detailed analysis. In Section II-B the efficiency and weight of the MV cable is investigated as a function of the operating voltage. Furthermore, low voltage (LV) and medium voltage (MV) versions of the generators are analyzed and the weight and efficiency of the two alternatives are compared. Further main points are the analysis of suitably adapted rectifiers/inverters and of a dc–dc converter for raising the rectified output voltage of a LV generator to the MV level, considerations on the choice of a reference potential, on electromagnetic compatibility and electrical protection devices for assuring a high system reliability. Then, in Section II-G the results of the analysis are discussed and a system structure favorable for the implementation of the demonstrator is selected and parameterized. To assure the practical feasibility of the concept, the control behavior of the system is modeled in Chapter III for generator and motor operation, a control structure is proposed and the control parameters are chosen with regard to stability and system dynamics. Finally, in Chapter IV the essential results of the work are summarized and an outlook on further research is given.

The work is supplemented by an Appendix which summarizes the aerodynamic fundamentals of CWTs and power kites in highly simplified form to enable the reader to make basic calculations and a comparison of the two concepts; finally, numerical values are given for the $100\,kW$ system discussed in this work.

## II. Power Kite Electrical System

In the following, as a first step, possible structures for the power kite electrical system are discussed; then the cable connection to the ground and the subsystems for two main concepts are analyzed. In conclusion, with regard to the overall system and efficiency, the final system structure is selected.

### A. Electrical System Structures

Because the AWT is planned to fly at $800 \ldots 1000\,m$, power transmission to the ground must be at MV in order to assure low electrical losses at low weight, i.e. low conductor cross-sections of the transmission cable. Here only direct current can be considered; a three-phase medium frequency transmission would lead to high reactive currents owing to the close proximity of adjacent conductors, and/or the high capacitance of the cable; single-phase alternating current is also eliminated owing to a power flow pulsating at twice the frequency, and the weight of the additional capacitive storage thus required.

Apart from the fundamental choice of the voltage level (which will be discussed in more detail in Section II-B), it is important to note that for determining the structure of the electrical system, or the configuration of the power electronics converters, apart from
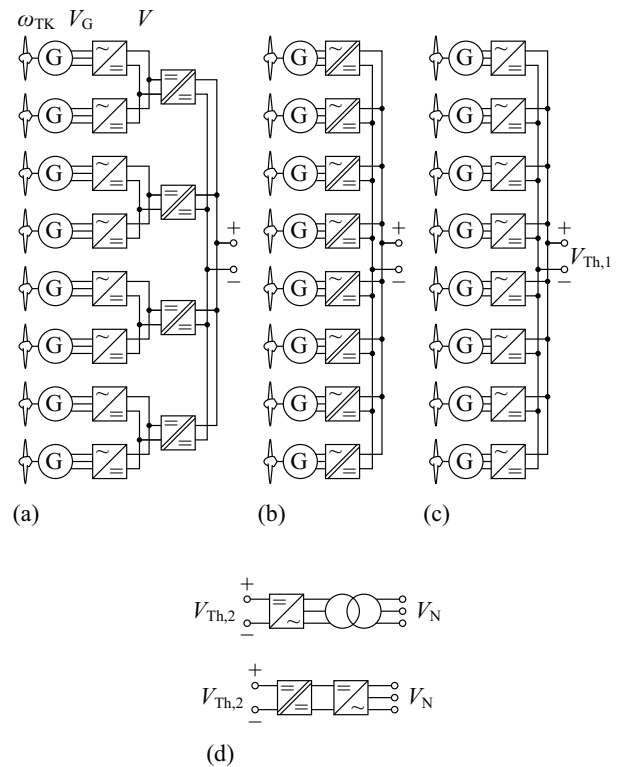


Fig. 6. Selection of possible concepts of AWT power electronics; (a), (b) LV generators, (c) MV generators; (d) possible structures of the ground station power electronics and connection to the three-phase mains.

generator operation, motor operation must also be managed for the takeoff and landing of the AWT. All the converter stages must hence be designed for bidirectional operation.

In order to obtain a high transmission voltage, direct series connection of the intrinsically potential-free generator outputs after rectification would be near at hand. Because of the mostly different wind conditions and hence different power and voltage generation of the individual generators and the potentially required motor operation of individual machines for control maneuvers, however, only a parallel connection of the subsystems is possible. The only possibility remaining is thus splitting the system into subgroups. Finally, the question remains whether the entire airborne power electronics (including the generators) should be designed for the transmission voltage level, or whether power generation and rectification should be done at low voltage. In the latter case, bidirectional dc–dc converters must be provided for coupling to the transmission cable, e.g. implemented as dual active bridge converters with MV output.

Possible concepts are shown in Fig. 6, whereby (a) and (b) are meant for LV generators and (c) for MV generators. For Fig. 6(a), as an alternative, the power of all generators could be collected via a LV dc bus and only a single coupling converter to the MV cable used. Splitting up as shown into 4 coupling converters, on the other hand, offers higher reliability and improved weight distribution over the aerofoil. For the system shown in Fig. 6(b), the rectifier stages and the coupling converters are integrated into individual single-stage three-phase ac–dc converters with high frequency isolation. However, the potentially lower weight of this system must be set against a considerably higher complexity as compared to Fig. 6(a). In addition, there is no possibility of e.g. integrating a battery storage for handling

emergencies such as landing during mains failure or rupture of the tether. For these reasons, this system is not pursued further for an initial analysis.

If the generators are implemented with MV output, an isolation in the coupling of the rectifier output to the MV cable can be avoided. However, because of the required insulation distances and the required implementation of the rectifier as a multi-level converter (with a larger number of power semiconductors, gate driver stages, etc.), a higher weight for both the generator and the converter must be expected. In order to be able to decide between LV [Fig. 6(a)] and MV generation [Fig. 6(c)], the main components for both concepts will be dimensioned and then the efficiencies and weights compared. Finally, the more favorable concept and its operating parameters will be chosen.

At the ground station, the power must be fed into the LV or MV grid at fixed voltage amplitude and frequency. In contrast to the airborne part of the system, weight and volume are here of secondary importance, so that a conventional industrial converter system can be employed. Hence for the sake of brevity, the power electronics implementation of the ground station will not be discussed further. It should only be pointed out that for coupling to the LV grid (400 V or 680 V line-to-line rms voltage), instead of a three-phase MV inverter with a transformer at the output, the dc–dc converter used on the aerofoil could be used with primary and secondary sides interchanged and a downstream LV inverter [cf. Fig. 6(d)]. This concept would have the advantage of higher control dynamics and would result in presumably lower realization costs, however at a (slightly) lower efficiency.

### B. Tether (Transmission Cable)

The tether represents a key element of an airborne wind turbine (AWT) power generation system. It retains the airborne part of the AWT system, i.e. the power kite, to the ground and provides the electric link between the kite's local power network and the ground-based power and control station, which is connected to the LV or MV grid. The requirements of the tether are demanding. Its desired properties can be summarized as follows:

- sufficiently high tensile strength and flexibility at a low weight to minimize the impact on the power kite's flight performance,
- failsafe transmission of electric power under repetitive mechanical strain to allow for high operational reliability and minimum maintenance, and
- resistance to environmental impacts such as UV irradiation, rain, or air pollutants in combination with water (leading to acid) to enhance the system lifetime.

Based on the requirements, three main components of the tether can be identified: a functional part that provides the tensile strength, two or multiple electric conductor(s), and a rugged outer protection jacket. The tether is comparable with a custom rugged and light-weight power transmission cable, where the most critical property is the weight. By investigating the materials of commercial power cables, it is found that the conductors, which are typically made of copper (Cu) or aluminum (Al), have the highest share of the weight. Thus, the cross sectional area of the conductors should be minimized to obtain a light-weight tether. This can be achieved by increasing the operating voltage, in this case the dc-voltage level. However, a higher operating voltage requires also a thicker insulation, which may ultimately lead to a higher weight again. This trade-off is the starting point of the following analysis.

To begin with, the tether construction has to be defined. One option is a design with coaxial electrical conductors at the tether's center.

Synthetic fibers would then surround the conductors and provide the physical strength necessary to withstand the pull of the kite system at a low weight. The disadvantage with a center aligned conductor (e.g. made of copper litz wire) is that the copper may yield under load. When the tensile force is relaxed, all parts of the tether behave elastically and retract apart from the copper, which is ductile and not elastic above 0.4% strain. The excess conductor length after ductile deformation has nowhere to go, and thus buckles and is likely to form a kink. A significantly better design is to use wire conductors that are arranged in a helical path around a center-aligned strain relief core. This provides the wire conductors some axial compliance when the cable is under tension or when load cycles are applied. A schematic cross section of the selected tether assembly (available e.g. from [16]) is depicted in Fig. 7. An alternative highly flexible cable construction, which is not further investigated here, is described in [17], [18].

The strain relief core is fabricated from aramid (Kevlar) fibers providing a tensile strength $\beta_{\mathrm{ts,Ar}} = 3.6\,\mathrm{kN/mm}^2$. Six copper or aluminum litz wires with cross-linked poly-ethylene insulation are considered for the conductors. An additional insulation layer could be added by wrapping an insulator material around the conductors. The outer tether protection jacket is implemented using a combination of elastomer and synthetic fiber layers (e.g. Hytrel thermoplastic elastomer and Vectran fibers manufactured by DuPont). The material data of the tether is summarized in Tab. I.

Firstly, the tensile strength of the tether needs to be determined. For that purpose it is assumed that the power kite is operated as shown in Fig. 35. The maximum force of the tether $F_{\mathrm{Th,max}}$ can then be estimated by

$$F_{\mathrm{Th,max}} = \frac{1}{2}c_{\mathrm{LK}}\rho A_{\mathrm{K,eff}}v_{\mathrm{W,r}}^2 \frac{v_{\mathrm{W,r}}}{\sqrt{v_{\mathrm{W,r}}^2 - v_{\mathrm{W}}^2}} . \tag{3}$$

Considering an effective kite wing area of $A_{\mathrm{K,eff}} = 25\,\mathrm{m}^2$ including the mounting of the generator/motor units, the maximum tether force yields to $F_{\mathrm{Th,max}} \approx 22.5\,\mathrm{kN}$. (The density of air is assumed with $\rho = 1.225\,\mathrm{kg/m}^3$, the lift coefficient of the kite wing with $c_{\mathrm{LK}} = 1.2$, the wind speed with $v_{\mathrm{W}} = 10\,\mathrm{m/s}$, and the relative wind speed acting upon the kite wing with $v_{\mathrm{W,r}} = 33.4\,\mathrm{m/s}$.) The required diameter of the aramid core $d_{\mathrm{c}}$, including a safety factor of three, can then be
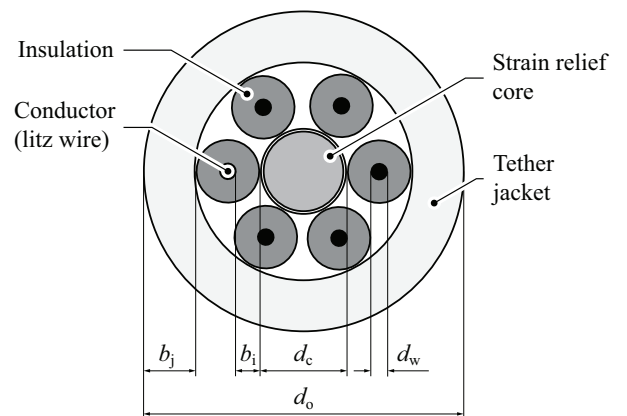


Fig. 7. Cross section of the designed tether, showing its assembly with a center-aligned strain relief core, six litz wire conductors with insulation arranged around the core, and the tether protection jacket. An additional insulation layer could be wrapped around all conductors.

calculated to

$$d_c = \sqrt{\frac{3 \cdot 4 F_{\text{Th,max}}}{\beta_{\text{ts,Ar}} \pi}} \approx 5\,\text{mm} . \qquad (4)$$

Next, the thickness of the cross-linked poly-ethylene conductor insulation $b_i$ needs to be expressed as a function of the insulation voltage $V_i$. The required relation is given by

$$b_i = 0.0144 \frac{\text{mm}}{\text{kV}^2} \cdot V_i^2 + 0.1694 \frac{\text{mm}}{\text{kV}} \cdot V_i + 0.40\,\text{mm} , \qquad (5)$$

and is determined based on the insulation layer thickness of commercial MV power cables for transportation systems [19]. The thickness of the tether protection jacket $b_j$ is assumed with $3\,\text{mm}$ and is kept constant within the considered tether parameter range. In order to determine the ohmic losses, the litz wire resistance $R_w$ at $20°\text{C}$ is modeled as a function of the wire diameter $d_w$ and the wire length $l_w$ using the data from [20],

$$R_w = \frac{1.7877 \cdot 10^6}{\sigma} \frac{1}{\text{m}} \cdot l_w \cdot \left(\frac{d_w}{\text{mm}}\right)^{-2.017} \qquad [\sigma] = \frac{S}{m} . \qquad (6)$$

$l_w$ is assumed with the length $l_{\text{Th}}$ of the tether. The remaining design variables of the tether are the litz wire diameter $d_w$ and the dc-voltage of the tether, e.g. $V_{\text{Th},1}$ at the connection point to the AWT. The tether is now fully parameterized and the optimal tether voltage can be determined by varying $V_{\text{Th},1}$. Thereby, the resulting wire resistance of the tether $R_{\text{Th}}$ is adapted such that the tether efficiency

$$\eta_{\text{Th}} = \frac{P_{\text{Th},1} V_{\text{Th},1}^2 - P_{\text{Th},1}^2 R_{\text{Th}}}{P_{\text{Th},1} V_{\text{Th},1}^2} \geq 97\% \qquad R_{\text{Th}} = \frac{2}{3} R_w \qquad (7)$$

remains constant and above a predefined minimum value. The ground-based power station with a dc-bus voltage $V_{\text{Th},2}$ ensures that the positive and negative bus is referenced to the ground potential by $\pm V_{\text{Th},2}/2$. This enables to design the conductor-to-ground insulation for $V_{\text{Th},2}/2$ only. The six conductors of the tether are alternately

TABLE I
TETHER MATERIAL DATA AND PARAMETER OVERVIEW.

| Property | Value | Description |
|---|---|---|
| $\beta_{\text{ts,Ar}}$ | $3.6\,\text{kN/mm}^2$ | Tensile strength of aramid (Kevlar) |
| $\rho$ | $1.225\,\text{mg/cm}^3$ | Density of air |
| $\rho_{\text{Al}}$ | $2.8\,\text{g/cm}^3$ | Density of aluminum |
| $\rho_{\text{Ar}}$ | $1.45\,\text{g/cm}^3$ | Density of aramid (Kevlar) |
| $\rho_{\text{Cu}}$ | $8.9\,\text{g/cm}^3$ | Density of copper |
| $\rho_{\text{PE}}$ | $0.92\,\text{g/cm}^3$ | Density of cross-linked poly-ethylene |
| $\rho_j$ | $1.3\,\text{g/cm}^3$ | Density of the tether jacket |
| $\sigma_{\text{Al}}$ | $3.5 \cdot 10^7\,\text{S/m}$ | Conductivity of aluminum |
| $\sigma_{\text{Cu}}$ | $5.96 \cdot 10^7\,\text{S/m}$ | Conductivity of copper |
| $b_i$ | $1.3\,\text{mm}$ | Thickness of the litz wire insulation |
| $b_j$ | $3\,\text{mm}$ | Thickness of the tether jacket |
| $d_c$ | $5\,\text{mm}$ | Strain relief core diameter |
| $d_w$ | $1.5\,\text{mm}$ | Litz wire diameter |
| $d_o$ | $19.2\,\text{mm}$ | Outer tether diameter |
| $F_{\text{Th,ts}}$ | $70\,\text{kN}$ | Tensile strength of the tether |
| $l_{\text{Th}}$ | $1000\,\text{m}$ | Tether length |
| $m'_{\text{Th}}$ | $0.32\,\text{kg/m}$ | Specific mass of the tether |
| $V'_{\text{Th},1}$ | $\leq 8\,\text{kV}$ | Tether voltage at the AWT system |
| $C'_{\text{Th}}$ | $100\,\text{pF/m}$ | Specific tether capacitance |
| $L'_{\text{Th}}$ | $360\,\text{nH/m}$ | Specific tether inductance |
| $R'_{\text{Th}}$ | $9\,\text{m}\Omega/\text{m}$ | Specific tether resistance |
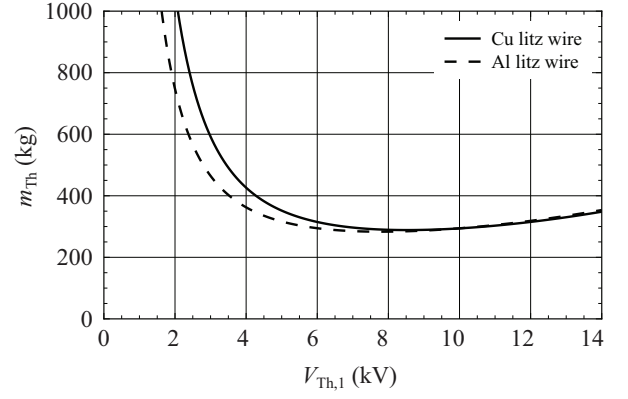


Fig. 8. Tether mass versus tether dc-voltage for copper (Cu) and aluminum (Al) litz wire conductors, for a fixed tether efficiency $\eta_{\text{Th}} = 98.5\%$ ($1.5\,\text{kW}$ conduction losses at a power input of $100\,\text{kW}$).
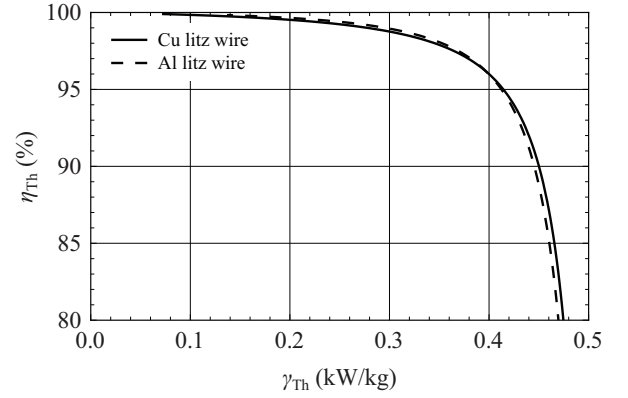


Fig. 9. Efficiency versus power-to-weight ratio of the tether for copper (Cu) and aluminum (Al) litz wire conductors at a tether dc-voltage of $8\,\text{kV}$.

connected to the positive and negative bus to reduce the resultant tether inductance.

Fig. 8 shows the relation between the tether weight and tether dc-voltage for copper and aluminum litz wire conductors, assuming a tether efficiency of $\eta_{\text{Th}} = 98.5\%$. This corresponds to $1.5\,\text{kW}$ conduction losses at a tether input power from the AWT system of $P_{\text{Th},1} = 100\,\text{kW}$ and a tether length of $l_{\text{Th}} = 1000\,\text{m}$. The optimal dc-voltage of the tether leading to the lowest weight is approximately $8\,\text{kV}$ as can be seen from Fig. 8. Aluminum wire conductors do not lead to a weight reduction. Thus, the tether is designed for a maximum nominal operating voltage of $8\,\text{kV}$ using copper litz wires. The resulting tether parameters are given in Tab. I. The outer tether diameter equals to $d_o = 19\,\text{mm}$, requires a litz wire diameter of $d_w = 1.5\,\text{mm}$ (corresponds to AWG 16), and has a specific mass of $m'_{\text{Th}} = 0.32\,\text{kg/m}$.

Finally, in Fig. 9 the tether efficiency is plotted versus the achievable power-to-weight ratio $\gamma_{\text{Th}}$, which is given by

$$\gamma_{\text{Th}} = \frac{P_{\text{Th},1} V_{\text{Th},1}^2 - P_{\text{Th},1}^2 R_{\text{Th}}}{V_{\text{Th},1}^2 m_{\text{Th}}} . \qquad (8)$$

These characteristics will be used later for the overall AWT power generation system optimization and indicates that the power-to-weight ratio should be selected below $0.4\,\text{kW/kg}$ for the considered tether design. Beyond $0.4\,\text{kW/kg}$, the copper cross section becomes too small leading to a steep drop in efficiency, and the tether weight is then mainly determined by the non-conductive materials.

## C. Generator / Motor

*1) Machine Type Selection:* The electrical machine is required to feature low weight together with high efficiency. Permanent magnet synchronous machines or brushless dc machines are known to perform best compared to machines with lower utilization factors such as induction machines and switched reluctance machines or also brushed dc machines which in addition suffer from poor reliability and high maintenance effort.

Permanent magnet machines reaching highest efficiencies are slotless type machines with air gap windings realized in both radial and axial flux configuration, however, achievable torque densities are smaller compared to their slotted counterpart. A radial flux machine with slotted stator and an internal rotor allows the stator mounted cooling fins being exposed to the airflow and therewith enables very effective cooling, for which reason it has also been chosen in [21]. Therefore, the internal rotor configuration is analyzed in the further investigation. The investigated machines use concentrated windings, which, despite a lower winding factor due to shorter end windings, generally have lower copper losses compared to motors with distributed windings [22].

For the LV machine dual layer concentrated windings are planned. For the MV machine single layer concentrated windings seem better applicable as the electrical insulation is only needed between the windings and the stator core. No extra insulation is needed between two different phases, as it would be the case in a dual layer configuration. A conceptual drawing of the two machines is shown in Fig. 10.

*2) Electromagnetic Models:* An analytical machine model is used to perform a weight and efficiency optimization to finally obtain optimal machine designs for a fair comparison of the LV and the MV concept. The machine model is predicated on a very basic estimate of the magnetic field in the air-gap ignoring slotting effects and assuming sinusoidal phase currents and infinite permeability of the stator iron and rotor yoke. The average torque for a radial flux permanent magnet machine can then be written as

$$T = R_{ag}LB_1JA_sk_{Cu}k_w\cos(\theta) , \qquad (9)$$

where $R_{ag}$ is the air-gap radius, $L$ is the active length, $B_1$ is the fundamental component of the open circuit radial flux density (rms) on the stator surface to the air-gap, $J$ is the current density in the winding conductors (rms), $A_s$ is the total area of all slots, $k_{Cu}$ is the copper fill factor, $k_w$ is the winding factor and $\theta$ is the phase
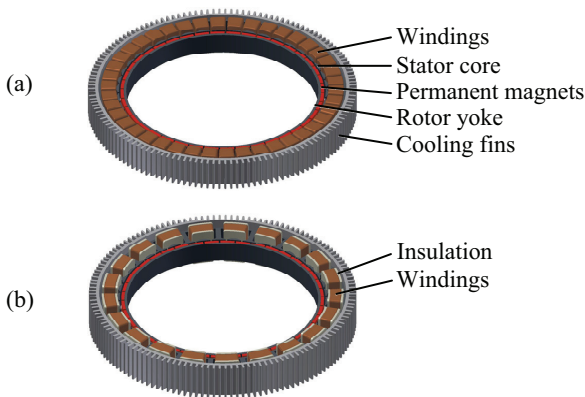


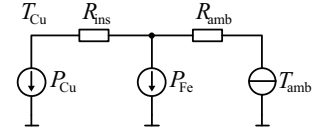Fig. 10. CAD drawing of (a) the LV machine and (b) the MV machine with extra insulation.



Fig. 11. Thermal equivalent circuit of the machine with resistive losses $P_{Cu}$ and iron losses $P_{Fe}$ and thermal resistance of the winding insulation $R_{ins}$ and thermal resistance to the ambient $R_{amb}$.

displacement of the back EMF voltage and the injected current vector.

To avoid magnetic saturation during operation, both the stator core and the rotor yoke geometry are chosen such that the materials are just at the limit to saturation for operation with maximum current. Hence the tooth width is determined by the maximum flux $\Psi_{z,max}$ resulting from the permanent magnet and the stator current and the saturation flux density of the material $B_{sat}$ as

$$d_z = \frac{\Psi_{z,max}}{B_{sat}} . \qquad (10)$$

In a similar way the pole shoe geometry and the yoke thickness are determined from the maximum expected flux in the respective region. Once the geometry of the stator core is known, the iron losses are obtained from the Steinmetz equation

$$P_{Fe} = V_s \cdot c \cdot f^\alpha \hat{B}^\beta , \qquad (11)$$

with the stator iron volume $V_s$, the electrical rotational frequency $f$, the peak flux density $\hat{B}$ and the Steinmetz coefficients $\alpha$, $\beta$ and $c$. The resistive losses in the copper windings are

$$P_{Cu} = \frac{V_{Cu}J^2}{\sigma_{Cu}(T_{Cu})} , \qquad (12)$$

where $V_{Cu}$ is the total copper volume and $\sigma_{Cu}(T_{Cu})$ is the electrical conductivity, which is depending on the conductor temperature $T_{Cu}$. With the two loss components the machine efficiency in motor operation is calculated as

$$\eta_{mot} = \frac{P_{mech}}{P_{mech} + P_v} , \qquad (13)$$

where $P_{mech}$ is the mechanical power and $P_v = P_{Cu} + P_{Fe}$ are the total losses. In generator operation, the efficiency is

$$\eta_{gen} = \frac{P_{mech} - P_v}{P_{mech}} . \qquad (14)$$

*3) Thermal Model:* A thermal model is required to guarantee machine temperatures within safe limits and to preclude thermally infeasible designs. A very accurate model usually implies detailed information which is not a priori known. Therefore, a basic model, depicted in Fig. 11, is used to determine the mean machine and winding temperature and/or to compute the temperature dependent resistive losses. The thermal equivalent circuit considers two heat sources namely the resistive and the iron losses, $P_{Cu}$ and $P_{Fe}$, the thermal resistance of the winding insulation $R_{ins}$, and the thermal resistance to the ambiance $R_{amb}$. The winding temperature can then be written as

$$T_{Cu} = P_{Cu} \cdot R_{ins} + (P_{Cu} + P_{Fe}) \cdot R_{amb} + T_{amb} , \qquad (15)$$

where $P_{Cu}$ is still depending on the conductor temperature. Combining with (12) and the thermal dependency of the electrical conductivity

$$\sigma_{Cu}(T_{Cu}) = \frac{\sigma_{Cu}(T_{ref})}{1 + \alpha_{Cu} \cdot (T_{Cu} - T_{ref})} \qquad (16)$$
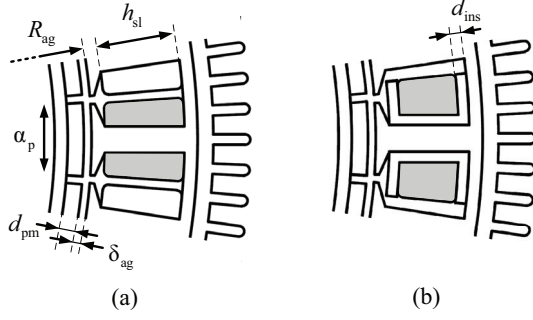
37

Fig. 12. Definition of machine dimensions for (a) the LV machine and (b) the MV machine with additional insulation; the windings around a stator tooth are highlighted in gray.



Fig. 13. Efficiency versus power density for the LV and the MV machines.

finally yields the resistive losses

$$P_{\mathrm{Cu}} = \frac{V_{\mathrm{Cu}} J^2 \cdot (1 + \alpha_{\mathrm{Cu}} \cdot (P_{\mathrm{Fe}} R_{\mathrm{amb}} + T_{\mathrm{amb}} - T_{\mathrm{ref}}))}{\sigma_{\mathrm{Cu}}(T_{\mathrm{ref}}) - \alpha_{\mathrm{Cu}} V_{\mathrm{Cu}} J^2 \cdot (R_{\mathrm{ins}} + R_{\mathrm{amb}})} , \qquad (17)$$

where $\alpha_{\mathrm{Cu}}$ is the copper conductivity temperature coefficient and $T_{\mathrm{ref}}$ is the reference temperature.

*4) Machine Optimization:* A grid search is performed to minimize the total mass of the active components

$$m = m_{\mathrm{Cu}} + m_{\mathrm{Fe,s}} + m_{\mathrm{Fe,r}} + m_{\mathrm{pm}} \qquad (18)$$

with the mass for the winding $m_{\mathrm{Cu}}$, stator iron $m_{\mathrm{Fe,s}}$, rotor iron $m_{\mathrm{Fe,r}}$ and permanent magnets $m_{\mathrm{pm}}$. The calculations for the efficiency are executed for two different operating points (OP), i.e. OP1, when the machine is used for power generation and OP2 for takeoff, when the machine is used as a motor. The power ratings and assumed ambient temperatures are listed in Tab. II. As a constraint, the maximum winding temperature is not allowed to exceed $100°$C. The optimization parameters and the parameter range used for the grid search are given in Tab. III. The parameter definitions are given in Fig. 12. For the stator iron, $0.2\,\mathrm{mm}$ cobalt-iron is used to obtain

TABLE II
MACHINE OPERATING POINTS

|  | Generator (OP1) | Motor (OP2) |
|---|---|---|
| Mechanical power $P_{\mathrm{mech}}$ | 16 kW | 16 kW |
| Rotational speed $n$ | 2000 rpm | 3000 rpm |
| Ambient temperature $T_{\mathrm{amb}}$ | $30°$C | $40°$C |

TABLE III
MACHINE OPTIMIZATION PARAMETERS AND FIXED PARAMETERS

| Optimization parameters | Symbol | Range |
|---|---|---|
| Air-gap radius | $R_{\mathrm{ag}}$ | $50\ldots250$ mm |
| Active length | $L$ | $10\ldots60$ mm |
| Slot depth | $h_{\mathrm{sl}}$ | $5\ldots20$ mm |
| Permanent magnet thickness | $d_{\mathrm{pm}}$ | $2\ldots8$ mm |
| Pole coverage factor | $\alpha_{\mathrm{p}}$ | $0.8\ldots1$ |
| Number of pole pairs | $p$ | $5\ldots30$ |

| Fixed parameters | Symbol | Value |
|---|---|---|
| Air gap | $\delta_{\mathrm{ag}}$ | $1.5$ mm |
| Copper filling factor | $k_{\mathrm{Cu}}$ | $0.45$ |
| Permanent magnet remanence | $B_{\mathrm{rem}}$ | $1.3$ T |
| Iron saturation flux density | $B_{\mathrm{sat}}$ | $2.2$ T |
| Insulation thickness (MV machine only) | $d_{\mathrm{ins}}$ | $2$ mm |

minimal iron losses at high flux densities. The maximum allowed electrical frequency is limited to $1500\,\mathrm{Hz}$ which, with the maximum rated speed of $3000\,\mathrm{rpm}$, permits a maximum pole pair number of $p = 30$.

For the two different machines, the obtained achievable efficiencies are plotted as a function of the power-to-weight ratio in Fig. 13. The LV machine is characterized by a maximum power-to-weight ratio of $3.23\,\mathrm{kW/kg}$ and/or shows only approximately half of the weight of the MV machine, which reaches a maximum power-to-weight ratio of $1.70\,\mathrm{kW/kg}$. In the same machine designs an efficiency of 95.1% is reached for the LV machine, while for the MV machine the efficiency is lower with 93.5%. Therefore, the MV machine and the MV ac–dc converter are excluded from further investigations.

*D. Voltage Source Rectifier (VSR)*

The power electronic interface between the generators and the LV dc-bus on the power kite is provided with active bidirectional, three-phase AC-DC voltage source rectifiers that allow for sinusoidal input currents. Two basic topologies are considered: the two-level (6-switch) voltage source rectifier (2L VSR), shown in Fig. 14, and the three-level neutral point clamped (NPC) voltage source rectifier (3L VSR), depicted in Fig. 15. Both circuit topologies are well known in industry. The two-level voltage source converter is the most widely used circuit topology for LV drive applications. The aim of the following investigation is to determine the trade-off between converter efficiency and its power-to-weight ratio and thereupon to decide on whether the two- or three-level VSR topology should be selected. The rectifier specifications and a component overview is compiled in Tab. IV.

The 2L VSR requires only six transistors and diodes and features low conduction losses. Power semiconductors with a blocking voltage $V_{\mathrm{BR}}$ of $1200\,\mathrm{V}$ are required for the considered nominal dc-bus voltage on the power kite of $V = 700\,\mathrm{V}$. Contrary to the 2L VSR, the 3L VSR can be implemented with $600\,\mathrm{V}$ power devices and thus allows for lower switching losses at switching frequencies above $10\,\mathrm{kHz}$. The 3L VSR typically has higher conduction losses than the 2L VSR due to the series connected transistors and diodes. $1200\,\mathrm{V}$ Si Trench&FieldStop (T&FS) IGBT4 devices and $1200\,\mathrm{V}$ SiC Schottky freewheeling diodes (ThinQ2 series) both from Infineon are considered for the 2L VSR to enable low losses at elevated switching frequencies, whereas for the 3L VSR, $600\,\mathrm{V}$ Si T&FS IGBT3 devices and $600\,\mathrm{V}$ Si EmCon3 diodes from Infineon are selected. A detailed comparison and semiconductor loss evaluation of the two- and three-
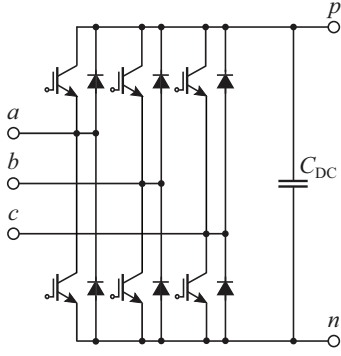
38

Fig. 14. Circuit topology of the two-level voltage source rectifier (2L VSR).
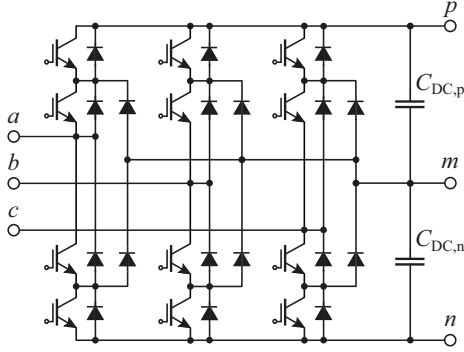


Fig. 15. Circuit topology of the three-level neutral point clamped voltage source rectifier (3L VSR).

level voltage source converter is presented in [23]. For both rectifier systems, discontinuous sinusoidal space vector modulation is applied as described in [23], [24].

The total losses of the VSR $P_{L,VSR,tot}$ are determined based on the total semiconductor losses $P_{Semi,VSR}$ and the total power consumption of the auxiliary supply, in which the power consumption of the gate drivers and the control and measurement circuitry is included.

$$P_{L,VSR,tot} = P_{Semi,VSR} + P_{aux,VSR} \qquad (19)$$

The power consumption of the auxiliary supply is assumed with $P_{aux,2L} = 8\,W$ for the 2L VSR and with $P_{aux,3L} = 12\,W$ for the 3L VSR. The overall efficiency $\eta_{VSR}$ is then given by

$$\eta_{VSR} = \frac{P_{G,VSR}}{P_{G,VSR} + P_{L,VSR}} \,, \qquad (20)$$

where $P_{G,VSR}$ corresponds to the power supplied/drawn by the generator/motor. In order to ensure sinusoidal currents at a maximum electrical frequency of $f_{G,max} = 1600\,Hz$, a minimum switching frequency of $f_{S,min} = 24\,kHz$ is assumed, which is a factor of 15 higher than $f_{G,max}$. A common basis for the semiconductor loss calculation is provided by determining the minimum semiconductor area according to the methodology presented in [24], [25] to meet the junction temperature requirements for both relevant operating points: rectifier (OP1) and inverter (OP2) operation at nominal apparent power. The semiconductor losses are then calculated for an average junction temperature of $T_J = 125°C$, a current-to-voltage displacement angle of $\Phi_{G,g} = \pi/6$ (generator operation) and $\Phi_{G,m} = 5\pi/6$ (motor operation) respectively, and an estimated generator/motor efficiency of $\eta_{G,est} = 96\%$. This yields to a nominal

apparent power (on the ac-side) of $S_{G,nom} = 19.3\,kVA$ for a shaft power of the generator/motor of $16\,kW$.

The next step is to identify and model the main components that contribute to the overall converter weight; these are the heat sink, the dc-link capacitors, the gate drivers, and the auxiliary supply including the measurement and control (DSP and/or FPGA) circuitry and the printed circuit board (PCB).

Forced air cooling is considered, where the air flow is taken from the propeller with an estimated air speed of $5\,m/s$. A bonded fin aluminum heat sink from Aavid Thermalloy (profile 69920) is considered. Based on these data the resulting specific mass of the heat sink is determined and a cooling system performance index [26] referenced to the mass $CSPI_m$ is introduced, which is defined as

$$CSPI_m = \frac{P_{CS,dis}}{\Delta T_{AS} m_{CS}} = \frac{1}{R_{th,CS} m_{CS}} = 15.0 \frac{W}{K\,kg} \,. \qquad (21)$$

This performance index describes the dissipated power $P_{CS,dis}$ of a cooling system as a function of the difference between ambient and sink temperature $\Delta T_{AS}$ and the mass $m_{CS}$ of the cooling system, i.e. the thermal conduction per unit mass.

The dc-link capacitance $C_{DC}$ is implemented with foil capacitors from EPCOS (3276x-series). For the 2L VSR, capacitors with a rated voltage of $800\,V$ and for the 3L VSR, capacitors with a

TABLE IV
RECTIFIER SPECIFICATIONS AND COMPONENT OVERVIEW.

| Property | Value | Description |
|---|---|---|
| $S_{G,nom}$ | 19.3 kVA | Nominal apparent power |
| $V_{G,ij,m}$ | 400 V | Line-to-line voltage at motor operation |
| $V_{G,ij,g}$ | 267 V | Line-to-line voltage at generator operation |
| $I_{G,m}$ | 27.8 A | ac current at motor operation |
| $\Phi_G$ | $0 \ldots 2\pi$ | Range of phase displacement |
| $\Delta I_{G,pp}$ | $\leq 0.2\,\hat{I}_{G,m}$ | Peak-to-peak ac current ripple |
| $V_{nom}$ | 700 V | Nominal dc-bus voltage |
| $V_{max}$ | 750 V | Max. dc-bus voltage |
| $M_m$ | 0.8 | Modulation index at motor operation |
| $M_g$ | 0.54 | Modulation index at generator operation |
| $f_{G,m}$ | 1500 Hz | Frequency at motor operation |
| $f_{G,g}$ | 1000 Hz | Frequency at generator operation |
| $f_{G,max}$ | 1600 Hz | Max. (electrical) frequency |
| $f_{S,min}$ | 24 kHz | Minimum switching frequency |
| $L_{S,max}$ | 2 mH | Max. inductance of a stator phase |
| $\eta_{G,est}$ | 96% | Estimated generator/motor efficiency |
| $T_{A,max}$ | 40°C | Max. ambient temperature |
| $T_{J,max}$ | 125°C | Max. junction temperature |
| $V_{BR,2L}$ | 1200 V | Si T&FS IGBT4, Infineon |
|  |  | SiC Schottky diodes, ThinQ2, Infineon |
| $V_{BR,3L}$ | 600 V | Si T&FS IGBT3, Infineon |
|  |  | Si EmCon3 diodes, Infineon |
| $P_{aux,2L}$ | 8 W | Input power of auxiliary for 2L VSR |
| $P_{aux,3L}$ | 12 W | Input power of auxiliary for 3L VSR |
| $C_{DC}$ | 120 µF | DC-link capacitance |
| $m'_{C,450}$ | 2 g/µF | Specific mass of 450 V foil capacitors |
| $m'_{C,800}$ | 4.8 g/µF | Specific mass of 800 V foil capacitors |
| $m_{aux}$ | 200 g | Mass of auxiliary circuitry and PCB |
| $m_{drv}$ | 20 g | Mass of a gate driver |
| $m_{PM,2L}$ | 50 g | Mass of power module for 2L VSR |
| $m_{PM,3L}$ | 75 g | Mass of power module for 3L VSR |
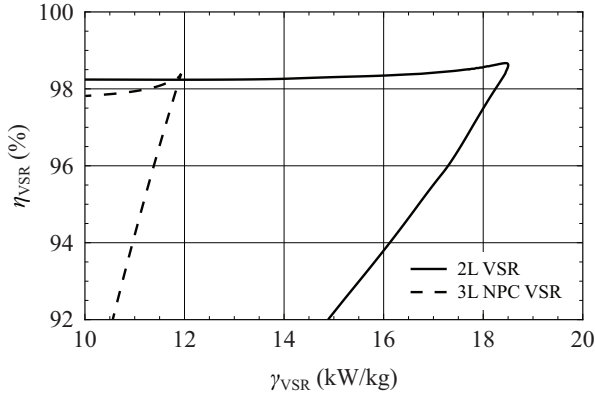
Fig. 16. Efficiency versus power-to-weight ratio of the 2L VSR and the 3L VSR. With the 2L VSR a significantly higher power-to-weight ratio at a similar maximum efficiency is achievable compared with the 3L VSR.

rated voltage of 450 V are considered, leading to a specific mass of $m'_{C,450} = 2\,\mathrm{g}/\mu\mathrm{F}$ and $m'_{C,800} = 4.8\,\mathrm{g}/\mu\mathrm{F}$ respectively. The dc-link capacitance is determined according to a control based criterion. Thereby, it is assumed that during flight operation the generator/motor has to be magnetized at maximum speed (1500 Hz) from a current level close to zero to nominal current for generator operation, when at that instant no power flow occurs across the terminals ($p$ and $n$) on the dc-side. The change of the dc-link capacitor voltage ($V_{\mathrm{nom}} = 700\,\mathrm{V}$) during this transient operation is limited to 25 V to provide a sufficient margin to the maximum dc-bus voltage $V_{\mathrm{max}} = 750\,\mathrm{V}$ for a maximum stator inductance value of $L_{\mathrm{S,max}} = 2\,\mathrm{mH}$ and a minimum switching frequency of $f_{\mathrm{S,min}} = 24\,\mathrm{kHz}$. A detailed description of this calculation can be found in [24]. The required minimum dc-link capacitance $C_{\mathrm{DC,min}}$ can then be calculated to $120\,\mu\mathrm{F}$, leading to a weight of the dc-link capacitor of 0.5 kg for the 2L VSR and 0.84 kg for the 3L VSR.

The mass of the power module including all three bridge-legs is assumed with $m_{\mathrm{PM,2L}} = 50\,\mathrm{g}$ for the 2L VSR and with $m_{\mathrm{PM,3L}} = 75\,\mathrm{g}$ for the 3L VSR based on data of respective power modules (EasyPACK, Infineon). The gate drives are considered in the weight calculation with $m_{\mathrm{drv}} = 20\,\mathrm{g}$ per piece. The remaining weight contribution of the auxiliary supply, the control and measurement circuitry, and the PCB is accounted for with $m_{\mathrm{aux}} = 200\,\mathrm{g}$.

The relation between the efficiency and the power-to-weight ratio of the 2L VSR and 3L VSR is determined by calculating first the semiconductor losses and then the total converter weight for a switching frequency range of 24 kHz to 70 kHz and a sink temperature range between 55°C and 100°C in order to find the optimal combination of parameters for the switching frequency and the sink temperature. The resultant characteristics are presented in Fig. 16. The results clearly show that the two-level VSR with Si IGBT4 devices and ThinQ2 SiC Schottky freewheeling diodes allows for a 50% higher power-to-weight ratio at a similar maximum efficiency of approximately 98.5% compared with the three-level NPC VSR using 600 V Si IGBT3 devices and Si EmCon3 diodes. The reason for this difference is that for the three-level VSR four times the dc-link capacitance of the two-level VSR is required due to the split dc-link capacitor ($C_{\mathrm{DC,p}}$ and $C_{\mathrm{DC,n}}$), whereas the ratio between the specific mass of the 800 V and the 450 V capacitors is only a factor 2.4 For this reason the two-level VSR is the topology of choice for the considered AWT generator/motor system.

*E. LV to MV DC–DC Converter*

The tether is operated with a high voltage of $\approx 8\,\mathrm{kV}$, in order to achieve a low tether weight (Section II-B). Thus, a bidirectional LV to MV dc–dc converter is needed to provide a power transfer between the LV dc bus (VSRs) and the MV port (tether); its specifications are listed below.

- Rated power: 100 kW in both directions of power transfer
- Nominal voltages: $V = 700\,\mathrm{V}$, $V_{\mathrm{Th,1}} = 7.5\,\mathrm{kV}$
- Input voltage range: $650\,\mathrm{V} < V < 750\,\mathrm{V}$
- Output voltage range: $6.9\,\mathrm{kV} < V_{\mathrm{Th,1}} < 8\,\mathrm{kV}$
- $V/V_{\mathrm{Th,1}}$ is constant in steady state: $V/V_{\mathrm{Th,1}} = 750\,\mathrm{V}/8\,\mathrm{kV}$
- Optimization target: low weight (the maximum allowable weight is set to 25 kg)

For the given application the modified Dual Active Bridge (DAB) converter topology shown in Fig. 17(a) is considered to be most suitable, in particular with respect to the low weight requirement, since it contains a low number of power components. Furthermore, the DAB facilitates equal power transfer characteristics in both directions due to its symmetric circuit structure.

The high frequency (HF) transformer and the inductor $L$ are the most heavy components of the DAB converter (cf. Tab. X). In order to reduce their weight, a high switching frequency is selected. The calculation of weight optimal DAB converters at different switching frequencies ($f_S = 50\,\mathrm{kHz}$, 80 kHz, 100 kHz, 125 kHz, 160 kHz, and 200 kHz) shows that a switching frequency of $f_S = 100\,\mathrm{kHz}$ leads to the best trade-off between HF losses (switching losses, core losses) and the weight of the converter.
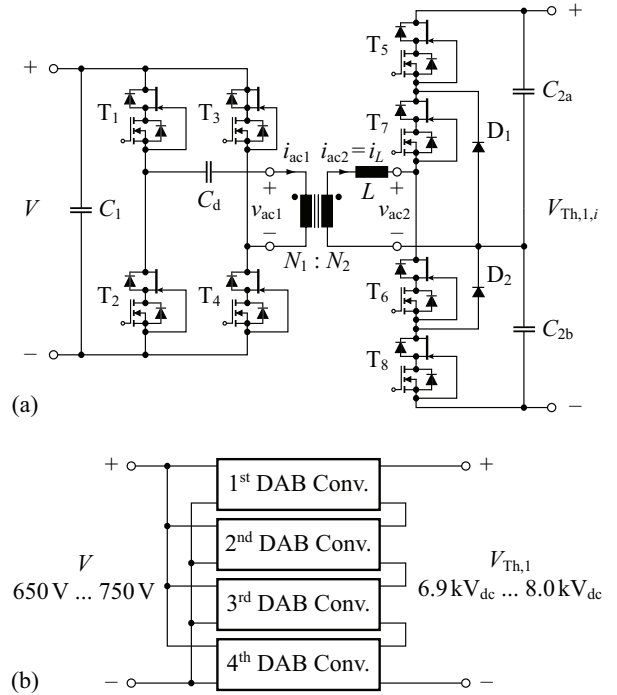


Fig. 17. (a) Single module of the considered DAB converter with a rated power of $P_i = 6.25\,\mathrm{kW}$, an input voltage range of $650\,\mathrm{V} < V < 750\,\mathrm{V}$ and an output voltage range of $1.6\,\mathrm{kV} < V_{\mathrm{Th,1,}i} < 2\,\mathrm{kV}$, whereas $V/V_{\mathrm{Th,1,}i} = 0.375 =$ constant in steady state operation; (b) proposed interconnection of 4 DAB converters to achieve a rated power of 25 kW at a MV port voltage range of $6.9\,\mathrm{kV} < V_{\mathrm{Th,1}} < 8\,\mathrm{kV}$. Four of the converters depicted in Fig. 17(b) are required to achieve an output power of 100 kW [cf. Fig. 6(a)]. The index $i$ used in Fig. 17(a) denotes the $i$-th DAB converter module shown in Fig. 17(b).
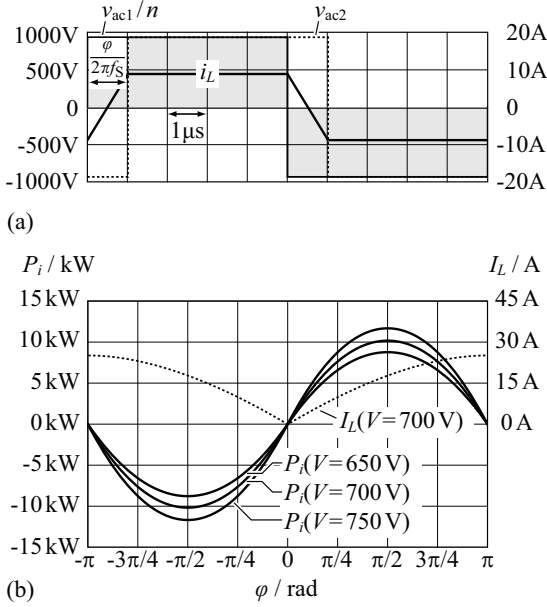
Fig. 18. (a) Voltage and current waveforms calculated for the lossless DAB converter defined in Tab. V and for $V = 700\,\text{V}$, $V_{\text{Th},1,i} = 2V/n = 1.9\,\text{kV}$, $P_i = 6.25\,\text{kW}/\eta_{\text{expected}}$, and $\eta_{\text{expected}} = 95\%$. (b) Power transfer characteristics of the DAB [calculated with (23)]; $V/V_{\text{Th},1,i} = 0.75/2 = \text{constant}$; maximum power transfer is achieved for $\varphi = \pm\pi/2$; the dashed line shows the rms inductor current $I_L(\varphi)$ at nominal operation.

In consideration of the high switching frequency and the rated voltage and power levels, SiC JFETs are required in order to achieve low switching losses. The selected SiC JFET (manufactured by SiCED/Infineon) is rated for a maximum voltage of 1200 V and is a normally-on device. However, the DAB converter shown in Fig. 17(a) requires switches with normally-off characteristics in order to ensure that a shoot-through in the bridge-legs is avoided. Therefore, the cascode connection with a LV MOSFET (IRLB8748PbF; rated voltage: 30 V), as shown in Fig. 17(a), is typically used; the LV MOSFET is selected with respect to a low on-state resistance and a low reverse recovery charge.

At the MV port a maximum voltage of 8 kV is specified. With the proposed neutral point clamped (NPC) converter shown in Fig. 17(a) a maximum port voltage of $V_{\text{Th},1,i,\text{max}} = 2\,\text{kV}$ is achieved. Four of these DAB converter modules are interconnected according to Fig. 17(b) [parallel connection of the LV side, series connection of the MV side; the index $i$ used in Fig. 17(a) denotes the $i$-th module shown in Fig. 17(b)] to achieve the total output voltage of 8 kV. The final system employs 4 of the converters depicted in Fig. 17(b), which are operated in parallel [cf. Fig. 6(a)]; thus, in total 16 DAB converter modules as shown in Fig. 17(a) are required. The selected SiC JFETs facilitate a rated power of $P_i = 100\,\text{kW}/16 = 6.25\,\text{kW}$ for a single DAB module.

The proposed DAB converter is operated most efficiently if the ratio between input and output voltages is equal to half of the turns ratio of the transformer,[1] i.e. $V/(V_{\text{Th},1,i}/2) = n = N_1/N_2$,

$$n = \frac{V}{V_{\text{Th},1,i}/2} = \frac{750\,\text{V}}{1\,\text{kV}} = 0.75 \; ; \tag{22}$$

[1] Only half of $V_{\text{Th},1,i}$ is applied to the transformer of the DAB due to the employed NPC bridge-leg structure at the MV side.

TABLE V
COMPONENT AND STRESS VALUES OF A SINGLE DAB CONVERTER MODULE WITH $P_i = 6.25\,\text{kW}/\eta_{\text{EXPECTED}}$ AND $\eta_{\text{EXPECTED}} = 95\%$.

| Property | Value | Description |
|---|---|---|
| $f_S$ | 100 kHz | Switching frequency |
| $n$ | 0.75 | Transformer turns ratio |
| $L$ | 107 $\mu$H | Converter inductance |
| $T_{\text{a,max}}$ | 40°C | Max. ambient temperature |
| $\max(V)$ | 750 V | Max. voltage at the LV port |
| $\max(V_{\text{Th},1,i})$ | 2 kV | Max. voltage at the MV port |
| $\max(I_{\text{ac1}})$ | 12.2 A | Max. rms transformer current, primary side |
| $\max(I_{\text{ac2}})$ | 9.2 A | Max. rms transformer current, secondary side |
| $\max(I_{\text{ac2,peak}})$ | 10.2 A | Max. peak inductor current |
| $\max(I_{\text{C1}})$ | 7.0 A | Max. rms capacitor current of $C_1$ |
| $\max(I_{\text{C2}})$ | 5.3 A | Max. rms capacitor current of $C_{2\text{a}}$ and $C_{2\text{b}}$ |

there, the conventional modulation scheme described in [27], often referred to as phase shift modulation, leads to the highest converter efficiency [28]. Fig. 18(a) shows typical voltage and current waveforms: $v_{\text{ac1}}$ and $v_{\text{ac2}}$ are rectangular, no freewheeling time interval is used; the phase shift $\varphi$ between $v_{\text{ac1}}$ and $v_{\text{ac2}}$ controls the output power of the DAB [27]:

$$P_i = \frac{V\,V_{\text{Th},1,i}/(2n)}{2\pi f_S L}\varphi\left(1 - |\varphi|/\pi\right) \; . \tag{23}$$

Equation (23) is used to determine the required inductance $L$:

$$L = \frac{\min[V\,V_{\text{Th},1,i}/(2n)]}{2\pi f_S P_{i,\text{max}}/\eta_{\text{expected}}}\varphi_{\text{max}}\left(1 - \varphi_{\text{max}}/\pi\right) \tag{24}$$

(an expected efficiency of $\eta_{\text{expected}} = 95\%$ is used). According to (23) the maximum power transfer is achieved for $\varphi = \pm\pi/2$. The rms inductor current $I_L$, however, continues to increase for $|\varphi| > \pi/2$ and reaches its maximum at $\varphi = \pi$, as shown in Fig. 18(b). Since $I_L$ causes copper losses in the transformer and inductor windings and conduction losses in all semiconductors [29], a maximum phase angle of $\pi/4$ is selected in order to achieve low losses.[2] Tab. V summarizes the component and stress values calculated for a single DAB converter module.

The DAB converter is designed with respect to minimum weight. The weight calculation, however, requires the converter losses to be known in order to determine the weights of the required heat sinks (separate heat sinks are considered for the LV side full bridge, the transformer and inductor, and the MV side NPC converter). The calculations of losses and weights are presented below and, subsequently, the design results for the minimum weight DAB converter are given.

*1) Calculation of the DAB's Losses:* The loss calculation considers conduction losses and switching losses of the semiconductor switches and the copper and core losses of the transformer and the inductor.

[2] For $\varphi_{\text{max}} = \pi/4$ a rms inductor current of 10 A is calculated at minimal voltages $V$ and $V_{\text{Th},1,i}$, whereas the rms current would be 13.3 A for $\varphi_{\text{max}} = \pi/2$ (there, $L = 143\,\mu$H applies); thus, the respective copper and conduction losses would increase by a factor of 1.8. The selection of a relatively small maximum phase angle, however, is only useful if the proposed DAB is operated close to $n = V/(V_{\text{Th},1,i}/2)$; a larger inductance (and thus, a larger maximum phase angle) yields better total performance if the operation within wide voltage ranges is required [29]. With a digital controller (100 MHz clock frequency and 10 ns minimum time step) the minimum phase angle is $\pi/500$ for $f_S = 100\,\text{kHz}$ and therefore, the minimum possible power transfer is 93 W for a single DAB converter module.
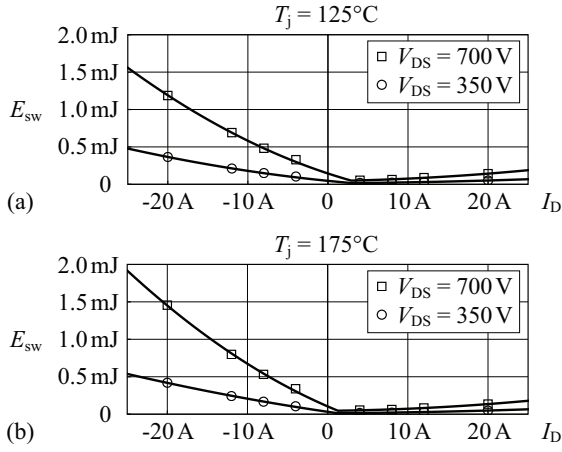
Fig. 19. Switching loss energy, which is dissipated in a single switching operation of the employed cascode connection of a 1200 V SiC JFET and a LV MOSFET (IRLB8748PbF) at (a) $T_j = 125°C$ and (b) $T_j = 175°C$. The □ and ○ symbols denote measured switching losses at different drain currents, $I_D$, and different drain-to-source voltages, $V_{DS}$, of the JFET. The solid line depicts the switching losses approximated by polynomial functions, which are parameterized using a least mean square approximation. Extrapolation is used to determine the switching losses for $V_{DS} > 700$ V. Moreover, $I_D > 0$ denotes soft switching and $I_D < 0$ denotes hard switching [29].

TABLE VI
PARAMETERS USED TO CALCULATE THE CONDUCTION LOSSES.

| $R_{DS,on}$ at $T_j = 25°C$ | $R_{DS,on}$ at $T_j = 150°C$ | Description |
|---|---|---|
| 80 mΩ | 150 mΩ | On-state resistance of the JFET |

| $R_{DS,on}$ at $T_j = 25°C$ | $R_{DS,on}$ at $T_j = 125°C$ | Description |
|---|---|---|
| 4.8 mΩ | 7.2 mΩ | On-state resistance of the MOSFET |

TABLE VII
STEINMETZ PARAMETERS OF N87 FERRITE MATERIAL AT A CORE TEMPERATURE OF 25°C (OBTAINED FROM DATA SHEET VALUES USING A LEAST MEAN SQUARE APPROXIMATION).

| Parameter | Value |
|---|---|
| $k$ | 14 |
| $\alpha$ | 1.72 |
| $\beta$ | 2.74 |

Tab. VI lists the on-state resistances of the employed JFET and the LV MOSFET, which are used to determine the conduction losses [30]. The conduction losses are calculated for a JFETs' junction temperature of 150°C and a MOSFETs' junction temperature of 125°C. Measured switching losses of the employed cascode connection, depicted in Fig. 19, are used to predict the switching losses of the DAB converter [29], [30].

The winding losses $P_{tr,wdg}$ and $P_{ind,wdg}$ of the transformer and the inductor are calculated with the respective rms currents and the ac winding resistances at a copper temperature of 100°C. The windings employ litz wires due to the HF operation, whereas a single strand copper diameter of $d_c = 0.071$ mm was found to yield the lowest resistance at $f_S = 100$ kHz.

The core losses of the employed N87 ferrite material are approximately determined with the Steinmetz equation,

$$P_{tr,core} \approx V_{tr,core} k f_S^\alpha B_{tr,peak}^\beta \text{ and } P_{ind,core} \approx V_{ind,core} k f_S^\alpha B_{ind,peak}^\beta , \quad (25)$$

TABLE VIII
DESIGN RESULTS OF A SINGLE DAB MODULE WITH A RATED POWER OF $P_i = 6.25$ kW$/\eta_{EXPECTED} = 6.6$ kW ($\eta_{EXPECTED} = 95\%$).

| Property | Value | Description |
|---|---|---|
| $\max(P_{LV,cond} + P_{LV,sw})$ | 79 W | Max. losses, LV side semiconductors |
| $\max(P_{MV,cond} + P_{MV,sw})$ | 68 W | Max. losses, MV side semiconductors |
| $\max(P_{tr,wdg})$ | 17 W | Max. copper losses, transformer |
| $\max(P_{ind,wdg})$ | 24 W | Max. copper losses, inductor |
| $\max(P_{tr,core})$ | 29 W | Max. core losses, transformer |
| $\max(P_{ind,core})$ | 8 W | Max. core losses, inductor |
| $\max(P_{tr,wdg} + P_{ind,wdg} + P_{tr,core} + P_{ind,core})$ | 70 W | Max. total losses of the transformer and the inductor |
| $P_{loss}(P_{in,i} = 6.6$ kW$)$ | 217 W | Total losses, full output power |
| $\eta_{loss}(P_{in,i} = 6.6$ kW$)$ | 96.7% | Efficiency, full output power |

whereas $V_{tr,core}$ and $V_{ind,core}$ denote the core volumes of the transformer and the inductor, respectively; $B_{tr,peak}$ and $B_{ind,peak}$ are the respective peak flux densities; $k$, $\alpha$, and $\beta$ are the Steinmetz parameters (given in Tab. VII). At a core temperature of $T_{core} = 25°C$ the core losses are higher than the losses at an elevated core temperature of $T_{core} = 100°C$. In order to account for increased core losses during the start-up phase of the converter $T_{core} = 25°C$ is considered. The different loss components of the DAB converter are listed in Tab. VIII.

*2) Weight Optimized Heat Sink:* The heat sink optimization procedure employs the equations presented in [26]. There, the optimal number of fins and the optimal fin thickness with respect to a minimum thermal resistance of the heat sink, $R_{th,heatsink}$, are calculated. The given application, however, requires the heat sink to be optimized with respect to minimum weight; here, the calculated losses and the specified temperatures determine the value of $R_{th,heatsink}$. Thus, the heat sink design procedure presented in [26] has been modified accordingly and yields a heat sink with a low number of fins in order to achieve minimum weight. Moreover, a relatively low thickness of the heat sink's base plate of $t_{baseplate} = 3$ mm is used to achieve a further weight reduction. The usability of the resulting heat sink has been verified with thermal FEM simulations.

*3) Calculation of the DAB's Weight:* Except for the transformer and the inductor all components can be selected based on the specifications and the stress values listed in Tab. V. The respective weights are listed in Tab. X and discussed below.

- The semiconductors' weights and the gate drivers' weights are measured values (the weight of the 2SC0435T gate driver, manufactured by Concept, is used as a reference value for $m_{LV,driver}$ and $m_{MV,driver}$).
- The PCBs' weights are estimated based on the expected board sizes.
- The capacitors' weights are estimated based on the capacitors' volumes ($C_1 = 6.8 \mu F$ (B32676G8685+000 from EPCOS); $C_{2a} = C_{2b} = 12 \mu F$ (B32776E1146+000, EPCOS); $C_d = 12 \cdot 560$ nF$/2$: ceramic capacitors (500 V / X7R capacitors from Syfer), which are connected in series and in parallel: 12 parallel × 2 series = 24 capacitors.
- The heat sinks' weights are calculated according to Section II-E2; for the sake of simplicity a fan is considered for each heat sink (the weight of the fan is given in Tab. IX). The heat sink for the LV side JFETs employs 8 fins with a length of 40 mm and a thickness of 1.1 mm; the size of the base plate is 40 mm × 47 mm. The heat sink of the MV side NPC converter employs 7 fins with a length of 40 mm and a thickness of 1.1 mm; the size of the base plate is 40 mm × 47 mm.

TABLE IX
PARAMETERS USED FOR THE TRANSFORMER DESIGN.

| Property | Value | Description |
|---|---|---|
| $B_{\text{tr,peak}}$ | 200 mT | Peak allowable flux density, transformer |
| $B_{\text{ind,peak}}$ | 200 mT | Peak allowable flux density, inductor |
| $k_{\text{tr}}$ | 0.85 | Max. fill factor, transformer |
| $k_{\text{ind}}$ | 0.75 | Max. fill factor, ind. (unusable space at air gap) |
| $b_{\text{iso,LVcore}}$ | 0.2 mm | Insulation width between LV wdg. and core |
| $b_{\text{iso,LVMV}}$ | 2 mm | Insulation width between LV and MV wdgs. |
| $b_{\text{iso,MVcore}}$ | 2 mm | Insulation width between MV wdg. and core |
| $b_{\text{cool}}$ | 0.3 mm | Thickness of the copper foil used for cooling |
| $h_{\text{iso,LVcore}}$ | 0.2 mm | Insulation height between LV wdg. and core |
| $h_{\text{iso,MVcore}}$ | 2 mm | Insulation height between MV wdg. and core |
| $d_{\text{heat pipe}}$ | 3.0 mm | Diameter of the heat pipe |
| $\Delta T_{\text{HS}}$ | 45°C | Assumed temperature difference between the Base plate of the heat sink and the air |
| $CSPI_{\text{m}}$ | $15\,\frac{\text{W}}{\text{kgK}}$ | Mass related Cooling System Performance Index |
| $m_{\text{fan}}$ | 50 g | Mass of the fan (San Ace 40, 9GV0142K301) |
| $m_{\text{heatpipe}}$ | 2 g | Mass of a single heat pipe, length: 80 mm |

The optimal design of the HF transformer and the inductor $L$, with respect to minimum weight and losses, requires an extensive optimization procedure. In a first step, the transformer and inductor setup is defined according to Fig. 20 in order to establish a scalable geometrical transformer and inductor model: Fig. 20(a) depicts the top view of the proposed configuration and Fig. 20(b) details the core window and defines the respective geometric properties. The transformer and the inductor employ $n_{\text{tr,core}}$ and $n_{\text{ind,core}}$ stacked E-cores, respectively, the LV winding is located close to the inner core leg, the MV winding is placed around the LV winding and encloses the transformer and the inductor cores, and the center core leg of the inductor employs an air gap to achieve the required converter inductance. A Teflon insulation with a thickness of 2 mm encloses the MV winding and a 0.2 mm thick insulation encloses the LV winding to achieve the isolation requirements of 100 kV. The copper foils and the heat pipes depicted in Fig. 20 are used to transport the dissipated heat from the windings and the core to the heat sink, which is placed on top of the configuration shown in Fig. 20(a). Moreover, an aluminum plate with a thickness of 3 mm is mounted to the bottom of the transformer and the inductor; it extracts the core losses from the bottom sides and uses the heat pipes depicted in Fig. 20(a) to transport the heat to the heat sink.

The employed design procedure calculates the weights and the losses of transformer and inductor for a high number of different designs. In order to reduce the computation time some constant design parameters, as listed in Tab. IX, are used. The remaining design parameter space is given with:

$$\vec{N}_1 = [5\ 6\ 7\ 8\ 9\ 10\ 11\ \dots\ 39\ 40]^{\text{T}},$$
$$\vec{N}_2 = \text{round}(\vec{N}_1 \cdot 1\,\text{kV}/750\,\text{V}),$$
$$\vec{n}_{\text{tr,core}} = [1\ 2\ 3\ 4\ 5\ 6\ 8\ 10\ 12\ 14\ 16\ 18\ 20]^{\text{T}},$$
$$\vec{n}_{\text{ind,core}} = [1\ 2\ 3\ 4\ 5\ 7\ 10]^{\text{T}},$$
$$\vec{a}_{\text{LVMV}} = [0.75\ 1.0\ 1.25]^{\text{T}},$$
$$\vec{c}_{\text{tr}} = [\text{E30/15/7}\quad \text{E32/16/9}\quad \text{E42/21/20}\quad \text{E55/28/21}$$
$$\text{E65/32/27}\quad \text{E70/33/32}\quad \text{UI93/76/30}\quad \text{UU93/76/30}]^{\text{T}},$$
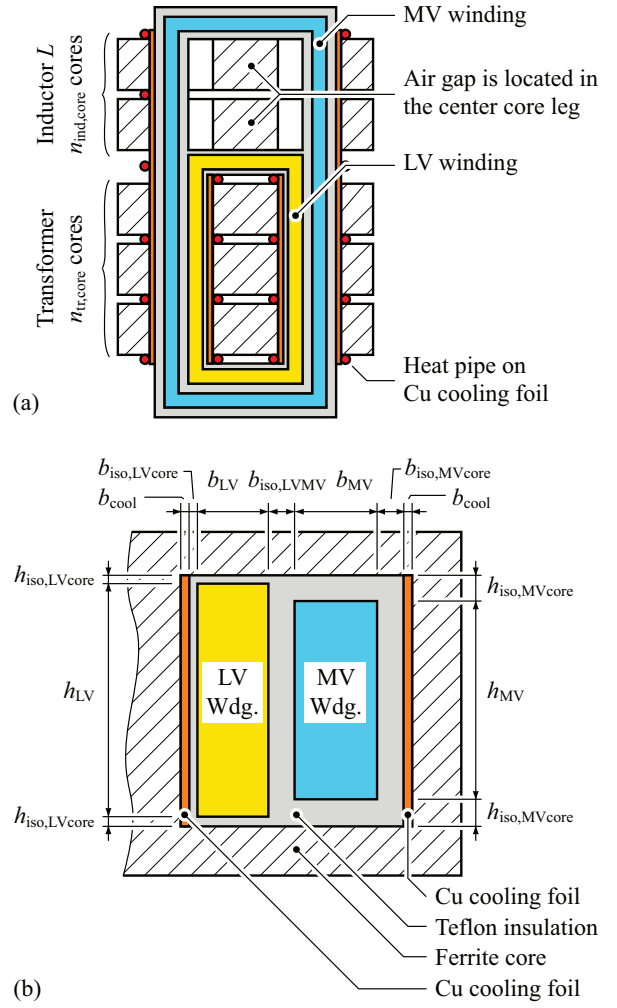$$\vec{c}_{\text{ind}} = \vec{c}_{\text{tr}} \tag{26}$$



Fig. 20. (a) Transformer setup with $n_{\text{tr,core}} = 3$ and $n_{\text{ind,core}} = 2$ as seen from top (cross-sectional drawing); the LV winding is located inside and encloses the 3 transformer cores; the MV winding is located around the LV winding due to the isolation requirements and encloses all 5 cores; the copper cooling foils and the heat pipes are used to extract copper and core losses and transport the losses to an external heat sink, which is mounted on top of transformer and inductor. (b) Cross-sectional drawing of the transformer winding window (front view); this Figure defines the geometric properties listed in Tab. IX.

($N_1$ the number of turns of the LV winding, $N_2$ the number of turns of the MV winding, $a_{\text{LVMV}}$ determines the ratio of the width of the LV winding and the width of the MV winding: $a_{\text{LVMV}} = b_{\text{LV}}/b_{\text{MV}}$; $\vec{c}_{\text{tr}}$ and $\vec{c}_{\text{ind}}$ contain the considered E cores). This parameter space still yields 78624 different designs. In order to reduce the number of stored design results, the employed design procedure, which is outlined in Fig. 21, conducts some tests, which are detailed below.

1) Does the MV winding, whose size is defined by the transformer core, fit into the selected inductor core?
2) Is the total weight of the selected cores reasonably low (e.g. less than 2.5 kg)?
3) Is the total weight of transformer and inductor reasonably small?
4) Is the peak flux density in the cores below a reasonable value (e.g. less than 200 mT at a switching frequency of 100 kHz)?
5) Is the total weight (transformer + inductor + heat sink) below a reasonable value?

43

TABLE X
WEIGHT OF A SINGLE DAB CONVERTER MODULE.

| Property | Value | Description |
|---|---|---|
| $m_{LV,semi}$ | 24 g | Total semiconductor mass, LV side |
| $m_{LV,driver}$ | 80 g | Total mass of the gate drivers, LV side |
| $m_{LV,PCB}$ | 40 g | Estimated mass of the PCB, LV side |
| $m_{C1}$ | 65 g | Estimated mass of $C_1$ |
| $m_{Cd}$ | 15 g | Estimated mass of the decoupling capacitor $C_d$ |
| $m_{LV,hs}+m_{fan}$ | 111 g | Heat sink and fan of the LV semiconductors |
| $m_{MV,semi}$ | 30 g | Total semiconductor mass, MV side |
| $m_{MV,driver}$ | 80 g | Total mass of the gate drivers, MV side |
| $m_{MV,PCB}$ | 50 g | Estimated mass of the PCB, MV side |
| $m_{C2a}+m_{C2b}$ | 130 g | Sum of the estimated mass of $C_{2a}$ and $C_{2b}$ |
| $m_{MV,hs}+m_{fan}$ | 106 g | Heat sink and fan of the MV semiconductors |
| $m_{tr}+m_{ind}$ | 481 g | Mass of the transformer and the inductor |
| $m_{tr,ind,hs}+$ $m_{fan}$ | 202 g | Mass of the heat sink used to cool transformer and inductor (including 14 heat pipes and fan) |
| $m_{DAB}$ | 1.414 g | Estimated mass of a single DAB module |

$$P_{tr,wdg}+P_{ind,wdg}+P_{tr,core}+P_{ind,core} \text{ (W)}$$



Fig. 22. Result of the transformer and inductor design; each point denotes the total weight and the maximum dissipated power calculated for a set of input parameters obtained from (26). The red points denote a total power loss density $p_{total}$ of less than $1.2\,\text{W/cm}^2$ (total dissipated power per available surface of the cooling foil shown in Fig. 20) and the gray points are the remaining results with $p_{total} \geq 1.2\,\text{W/cm}^2$. The dashed lines denote the estimated Pareto Fronts for $p_{total} < 1.2\,\text{W/cm}^2$ (red) and $p_{total} \geq 1.2\,\text{W/cm}^2$ (gray).
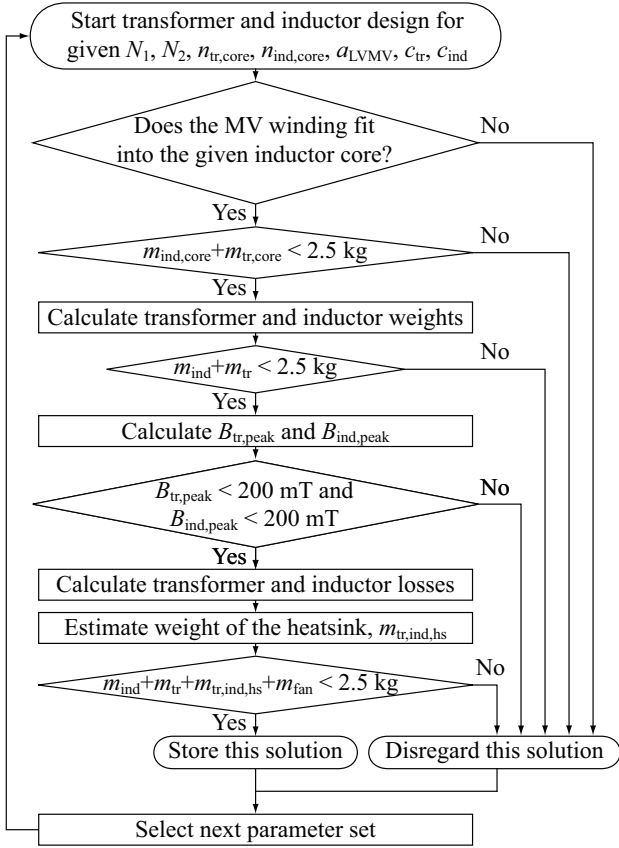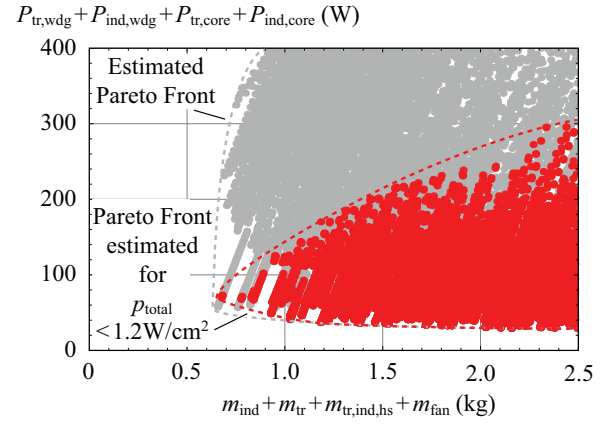


Fig. 21. Flowchart showing the procedure employed to design the HF transformer and the inductor of the DAB. With this design procedure the results shown in Fig. 22 are calculated.

The result of the transformer and inductor design is shown in Fig. 22. There, each point denotes the total weight and the total dissipated power calculated for a set of input parameters; the red points denote results with a total power loss density $p_{total}$ of less than $1.2\,\text{W/cm}^2$ ($p_{total}$ is the total dissipated power per available surface of the cooling foil shown in Fig. 20) and the gray points yield

$p_{total} \geq 1.2\,\text{W/cm}^2$. The dashed lines in Fig. 22 denote the estimated Pareto Fronts for $p_{total} < 1.2\,\text{W/cm}^2$ (red) and $p_{total} \geq 1.2\,\text{W/cm}^2$ (gray). According to the depicted Pareto Fronts, a loss reduction is possible by increasing the weight; however, due the side conditions considered in Fig. 21, also the maximum losses are limited at a certain weight. The design results for the most lightweight transformer and inductor design with $p_{total} < 1.2\,\text{W/cm}^2$ is listed below.

- Transformer core: 2 stacked E42/21/20 core sets
- Inductor core: one E42/21/20 core set
- Number of turns: $N_1 = 21$, $N_2 = 28$
- Employed litz wire, LV side: $151 \times 0.071\,\text{mm}$
- Employed litz wire, MV side: $132 \times 0.071\,\text{mm}$
- Inductor air gap length: $l_{air} = 2.3\,\text{mm}$

The maximum copper temperatures are calculated for minimum input and output voltages: $T_{tr,wdg,MV,max} = 149°\text{C}$ and $T_{tr,wdg,LV,max} = 135°\text{C}$ inside the MV winding and the LV winding, respectively. The maximum temperatures at nominal operation are $T_{tr,wdg,MV,max} = 131°\text{C}$ and $T_{tr,wdg,LV,max} = 120°\text{C}$.[3]

*F. EMI, Grounding, and Safety Concept*

*1) EMI and Grounding:* The considered electric system of an AWT consists of multiple switched power electronic converters. In order to ensure safe operation, electromagnetic interference (EMI) between the individual subsystems needs to be minimized and a suitable grounding concept should be applied. The airframe and surface of an AWT is typically constructed of non-conducting composite materials for weight purposes. A light-weight wire grid should therefore be implemented on the airframe to provide a possibility for grounding the individual converters and/or subsystems and to ensure an equalization of the electrostatic potential. This grounding grid could be connected to charge drainers, mounted e.g. on the surface of the wing, to prevent electrostatic charging as no reference potential is available the on the AWT due to the galvanic isolation provided by the dc–dc converters.

---

[3]For the litz wire a relatively low thermal conductivity of $\lambda_{Litz} = 0.22\,\text{W/(m K)}$ is assumed and needs to be verified with a measurement.

Ideally, shielded cables should be used between the LV terminals of the DAB and the dc terminals of the 2L VSRs and between the MV terminals of the DAB and the connection point to the tether as harmonics with switching frequency are injected into the LV and MV bus. This allows for a considerable reduction of the radiated EMI. Optionally, a common-mode filter could be placed on the dc-side of each VSR to reduce conducted EMI and lower the CM currents on the AWT. This filter would then be referenced to the grounding grid by CM capacitors.

*2) Safety Concept:* Another important aspect to be considered is the safety concept of an AWT. For this purpose the failure modes of the entire AWT power generation system have to be analyzed. In the following three characteristic faults are briefly discussed:

- mains failure at the ground-based power and control station,
- failure of a generator/motor unit, and
- rupture of the tether.

The mains failure can be handled by installing a ground-based USV system designed to provide sufficient power to enable a safe landing of the AWT. For safety purpose, either an energy storage (battery) and/or a pulsed resistor unit has to be installed that allows to absorb the power supplied from the AWT as no power can be supplied to the grid.

A generator/motor unit could fail due to electro-mechanical malfunction or due to a failure of the power electronics. The considered AWT system has eight turbines and thus requires eight VSRs, where always two VSRs are supplied by a DAB. The LV connections between the DAB and the VSRs could be protected with lead fuses in the considered wiring concept. If one generator/motor and/or VSR fail such that an over-current occurs on the LV dc-bus, the corresponding fuse trips and disconnects the VSR from the LV dc-bus. The second VSR, which is connected to the same DAB, can then still be operated, theoretically even above the nominal power level. An (electronic) over-current protection switch could be placed at the MV terminals of the DAB in order to minimize the impact of such a failure on the other motor/generator units. The protection switch does not only enable to disconnected the DAB during a failure transient and to reconnect it after successful recovery but can be also used to permanently disconnect the DAB from the MV dc-bus (tether) if the DAB itself fails. For safety purposes, a pulsed resistor should be placed at the LV terminals of the DAB.

The break of the tether is the most critical failure. The AWT then becomes an autonomous aircraft, which means that local computational power and sensors to determine the flight attitude are required to cope with this failure mode. One option would be to install a battery on the AWT, which would be only half-charged and thus could supply/absorb energy to/from the generator/motor units and thus enable an autonomous landing of the AWT. The disadvantage with this approach is the additional weight of the battery. If an autonomous emergency landing should be achieved without local energy storage, some of the generator/motor units could be operated as generators (similar to a RAM turbine of an aircraft) and some as motors and thus provide the required energy for a controlled landing.

### G. Evaluation and System Structure Selection

The above presented Pareto Fronts of the generator, the VSR, and the DAB converter facilitate the overall optimization of the kite's on-board electric system in order to determine the optimal dimensioning of the different system components (regarding the components' power-to-weight ratios and efficiencies) for a given overall power-to-weight ratio, $\gamma$, or a given overall efficiency, $\eta$, of the system. This optimization considers the block diagram depicted
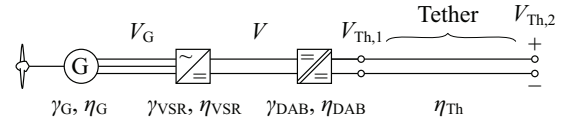


Fig. 23. Simplified block diagram of the kite's on-board electric system used for the overall system optimization.

in Fig. 23, which subsumes all 8 generators and VSRs to a single generator and a single VSR. The overall efficiency of this system is:

$$\eta = \eta_G\,\eta_{VSR}\,\eta_{DAB}\,\eta_{Th}\ . \tag{27}$$

The overall power-to-weight ratio is calculated by means of the different components' weights,

$$m = m_G + m_{VSR} + m_{DAB}\ , \tag{28}$$

$$m_{DAB} = \frac{P_{out}/\eta_{Th}}{\gamma_{DAB}(\eta_{DAB})}\ , \quad m_{VSR} = \frac{\frac{P_D}{P_R}\,P_{out}}{\eta_{DAB}\,\eta_{Th}}\,\frac{1}{\gamma_{VSR}(\eta_{VSR})}\ ,$$
$$m_G = \frac{\frac{P_D}{P_R}\,P_{out}}{\eta_{VSR}\,\eta_{DAB}\,\eta_{Th}}\,\frac{1}{\gamma_G(\eta_G)}\ , \tag{29}$$

$$\gamma = \frac{P_{out}}{m}\ . \tag{30}$$

In (29), the implications of the efficiencies on the particular components' weights are considered; moreover, generator and VSR are over-dimensioned by a factor of $P_D/P_R$,

$$P_D/P_R = 8 \cdot 16\,\text{kW}/100\,\text{kW} = 1.28\ , \tag{31}$$

in order to account for power fluctuations among the 8 generators and VSR. It can be seen from (28) and (29) that $P_{out}$ cancels out in (30); thus, $\gamma$ is independent of $P_{out}$.

The optimization with respect to $\gamma$ and $\eta$ aims to find the respective Pareto Front. Thus, regarding (28) and (29), a reduction of the computational effort is achieved if (29) is solely evaluated along the Pareto Fronts of $\gamma_G(\eta_G)$, $\gamma_{VSR}(\eta_{VSR})$, and $\gamma_{DAB}(\eta_{DAB})$:

$$\gamma_G(\eta_G) \to \gamma_{G,PF} = \max[\gamma_G(\eta_G)]$$
$$\gamma_{VSR}(\eta_{VSR}) \to \gamma_{VSR,PF} = \max[\gamma_{VSR}(\eta_{VSR})] \tag{32}$$
$$\gamma_{DAB}(\eta_{DAB}) \to \gamma_{DAB,PF} = \max[\gamma_{DAB}(\eta_{DAB})]\ .$$

The presented results employ polynomial estimations for $\gamma_{G,PF}$, $\gamma_{VSR,PF}$, and $\gamma_{DAB,PF}$; the data presented in the above sections for $\gamma_G(\eta_G)$, $\gamma_{VSR}(\eta_{VSR})$, and $\gamma_{DAB}(\eta_{DAB})$ is used to parameterize these polynomials by means of least mean square optimization.

Fig. 24 depicts the results for $\gamma$ and $\eta$ obtained from (27) to (32); a grid search algorithm is used to calculate the depicted data. The maximum achievable power-to-weight ratio of the on-board electrical system (power converters and generator/motor) is $\gamma_{max} = 1.39\,\text{kW/kg}$ at $\eta = 89.5\%$. However, the design with a slightly decreased power-to-weight ratio of $\gamma = 1.37\,\text{kW/kg}$, marked with a circle in Fig. 24(a), yields a notely higher efficiency of $\eta = 90.0\%$ and is therefore considered to be more suitable. With this, $m = 73\,\text{kg}$ results for a rated power of $100\,\text{kW}$. Fig. 24 also shows the design targets for a more efficient system design, marked with a circle: for $\gamma = 1.00\,\text{kW/kg}$ the efficiency increases to $\eta = 91.7\%$, however, the weight increases to $m = 100\,\text{kg}$. Tab. XI lists the respective design targets for the generator, the VSR, and the DAB converter.

Fig. 24.   (a) Calculated results for $\eta$ and $\gamma$ (overall system). The maximum power-to-weight ratio is $\gamma = 1.39\,\text{kW/kg}$; the selected design points are marked with □ and ○ symbols. (b) Pareto Fronts of the generator/motor, the VSR, and the DAB converter, which are used to compute the data of Fig. 24(a); the design points marked with □ and ○ correspond to the design points of Fig. 24(a). The Pareto Fronts of Fig. 24(b) are calculated for nominal operating voltages and rated power.

TABLE XI
EFFICIENCIES AND POWER-TO-WEIGHT RATIOS AT THE 2 DESIGN POINTS
MARKED IN FIG. 24(A) (CALCULATED FOR NOMINAL OPERATION).

| Total system | Generator, VSR, and DAB converter | | |
|---|---|---|---|
| $\gamma = 1.37\,\text{kW/kg}$ $\eta = 90.0\%$ | Generator: | $\gamma_G = 3.11\,\text{kW/kg}$, | $\eta_G = 95.4\%$ |
| | VSR: | $\gamma_{VSR} = 18.3\,\text{kW/kg}$, | $\eta_{VSR} = 98.6\%$ |
| | DAB: | $\gamma_{DAB} = 4.60\,\text{kW/kg}$, | $\eta_{DAB} = 97.1\%$ |
| $\gamma = 1.00\,\text{kW/kg}$ $\eta = 91.7\%$ | Generator: | $\gamma_G = 2.14\,\text{kW/kg}$, | $\eta_G = 96.9\%$ |
| | VSR: | $\gamma_{VSR} = 18.3\,\text{kW/kg}$, | $\eta_{VSR} = 98.6\%$ |
| | DAB: | $\gamma_{DAB} = 3.53\,\text{kW/kg}$, | $\eta_{DAB} = 97.4\%$ |

## III. POWER KITE ELECTRIC SYSTEM CONTROL

When considering the control concept of the electric and/or power electronic system, it is important to define what quantities should be controlled and which actuator should be used to do so. There are several control goals which can be divided roughly into

- flight attitude control,
- energy generation, and
- control of the dc-voltages.

The flight control can be handled by adjusting the speed of the individual machines and is a topic out of the scope of this paper. Therefore, each individual machine needs at least a separate speed control algorithm which tracks reference values related to flight commands transmitted over a probably wireless communication channel. The flight commands could be processed by a controller adjusting the flight attitude of the kite by generating the individual speed references.

TABLE XII
SUMMARY OF EQUIVALENT CIRCUIT COMPONENT VALUES.

| Parameter | Value | Description |
|---|---|---|
| $L_b$ | $40\,\text{mH}$ | Boost inductance of the ground based converter |
| $C_2$ | $20\,\mu\text{F}$ | DC-link capacitance at the ground station |
| $L_{Th}$ | $360\,\mu\text{H}$ | Inductance of the tether |
| $R_{Th}$ | $8\,\Omega$ | Resistance of the tether |
| $C_1$ | $6\,\mu\text{F}$ | Total capacitance at the MV port of all DABs |
| $C$ | $1070\,\mu\text{F}$ | Total capacitance at the LV port (VSRs + DABs) |
| $C_{1,eq}$ | $15.3\,\mu\text{F}$ | Input capacitance at the MV port ($C_1 + n_t^2 C$) |

The second objective is to generate a certain amount of energy. Basically all or some of the machines will then be controlled to have a certain breaking torque. Additionally, a superior maximum power point tracker could be used which adjusts the rotor speeds in such a way that maximum power can be extracted for a given wind speed.

All these controllers directly adjust the machines speed or torque and ultimately rely on a stable dc-link voltage. Whether energy is consumed by the machines in order to fly to the required position or if power is generated and supplied to the grid should have no influence on the dc-link voltage level. Abrupt changes in the energy flow direction should not lead to severe distortions and over-voltages because of the limited voltage rating of the dc–dc converter and the MV cable. Therefore, the dc-link voltage should be tightly controlled to stay in a predefined range.

For simplicity and reliability reasons, the ac–dc converter at the ground station is chosen to control the dc-link voltage. All remaining converters do not actively support or control the dc-link voltage and can be regarded as disturbing loads. The control objectives are mainly given by the voltage constraints of the dc–dc converter and the MV transmission cable. The LV bus should remain in the range of $650 \ldots 750\,\text{V}$ and the corresponding MV cable voltage should not exceed $8\,\text{kV}$ in response to load or reference changes. Voltage reference changes are uncritical because they can be adjusted with a reference filter. Therefore, the main objective is a controller design, for disturbance rejection and good damping.

In order to derive the necessary transfer functions for the controller design some approximations can be made which reduce the system complexity greatly. The whole system can be represented with the equivalent circuit depicted in Fig. 25(a). It consists of a three-phase ac–dc MV converter at the ground station (three-level topology with a switching frequency of $4\,\text{kHz}$), the MV cable, a bidirectional dc–dc converter and a current source representing the generator/motor units.

Although there are actually four $25\,\text{kW}$ dc–dc converters each connected to two machines, they can be combined to a single equivalent $100\,\text{kW}$ converter. It can then be assumed that it operates as an ideal transformer with a fixed voltage transfer ratio $n_t$. Because of its high switching frequency of $f_S = 100\,\text{kHz}$, this assumption is justified in the interesting frequency range.

The eight generator/motor units (probably operated in generator mode) can be combined to a single equivalent current source. The worst case scenario can be captured with step changes of this current source although this will unlikely happen because of the total rotor inertias and the rather low generator/motor speed control bandwidth. The bus voltage is supported in front of each machine with a capacitance of $C_m = 120\,\mu\text{F}$ which can be combined together with the LV side capacitor of the dc–dc converter to form the equivalent capacitance of $C = 1070\,\mu\text{F}$.
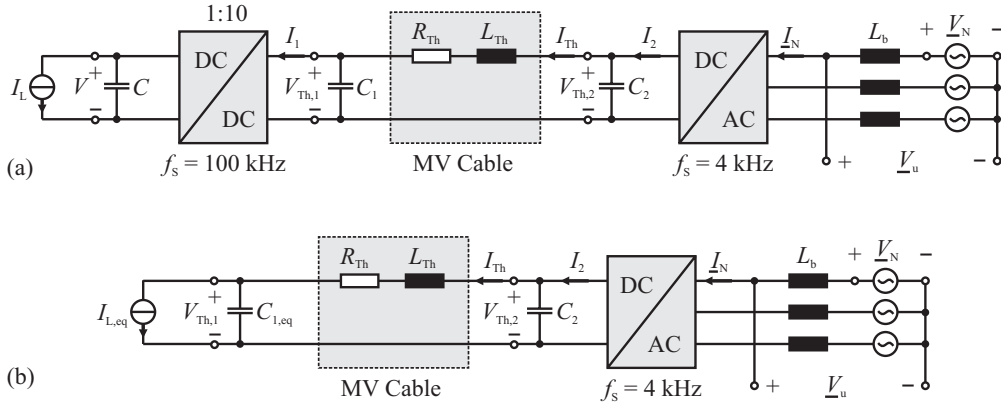
Fig. 25. Equivalent circuit of the AWT power electronic system.

The MV cable is represented with its series inductance $L_{Th}$ and resistance $R_{Th}$. The cable is terminated at the dc–dc converter and at the ground station with the capacitors $C_1$ and $C_2$ respectively. The cable capacitance itself is small and can be equally split and added to $C_1$ and $C_2$. The cable resonances are highly damped because of the rather high series resistance. The element values of the equivalent circuit are summarized in Tab. XII.

A further simplification can be made if the dc–dc converter is assumed to be an ideal transformer. So the capacitance $C$ and the current source representing the load can be transformed to the MV side as depicted in Fig. 25(b). Thereby, the ac quantities are split into their d- and q-components.

$$C_{1,eq} = C_1 + n_t^2 \cdot C \tag{33}$$

$$I_{L,eq} = n_t \cdot I_L \tag{34}$$

$$n_t = 700/7500 \tag{35}$$

Now, it is possible to derive the transfer functions for reference tracking and disturbance rejection. The respective equation system can be derived from the electrical equivalent circuit.

$$L_b \frac{dI_{Nd}}{dt} = V_{Nd} - V_{ud} \tag{36}$$

$$C_2 \frac{dV_{Th,2}}{dt} = I_2 - I_{Th} \tag{37}$$

$$L_{Th} \frac{dI_{Th}}{dt} = V_{Th,2} - V_{Th,1} - R_{Th} I_{Th} \tag{38}$$

$$C_{1,eq} \frac{dV_{Th,1}}{dt} = I_{Th} - I_{L,eq} \tag{39}$$

$$V_{Th,2} \cdot I_2 = \frac{3}{2} V_{ud} \cdot I_{Nd} \tag{40}$$

The ac voltages and currents are separated into d- and q-component values, e.g. $V_{Nd}$ is the d-component of the ac line voltage $\underline{V}_N$. The only nonlinear equation is the power transfer over the ac–dc converter [(40), it is assumed that the grid current q-component $i_{Nq}$ is controlled to zero] which has to be linearized around the steady state operating point.

$$i_2 = \frac{3}{2} \frac{I_{Nd,0}}{V_{Th2,0}} \cdot v_{ud} + \frac{3}{2} \frac{V_{ud,0}}{V_{Th2,0}} \cdot i_{Nd} - \frac{3}{2} \frac{V_{ud,0} I_{Nd,0}}{V_{Th2,0}^2} \cdot v_{Th,2} \tag{41}$$

First, a fast inner current control loop is designed to control the current vector in the 3-phase boost inductor $L_b$. A simple approach uses a PI controller $R_i$ for the current d- and q-components. Decoupling and feedforward of the grid voltage is used to derive the open-loop transfer function $G_{i,ol}$ which includes a dead time element

accounting for the time delays related to the PWM modulation and the processing time. The ac–dc converter is assumed to be operated at a switching frequency of $f_S = 4\,\text{kHz}$, and thus a time delay of approximately $T_t = 1/f_S = 250\,\mu\text{s}$ has to be considered.

$$G_{i,ol} = \frac{i_{Nd}}{v_{ud}} = \frac{1}{sL_b} e^{-sT_t} \tag{42}$$

$$G_{i,cl} = \frac{i_{Nd}}{i_{Nd,ref}} = \frac{R_i \cdot G_{i,ol}}{1 + R_i \cdot G_{i,ol}} \tag{43}$$

$$R_i = k_{pi} \frac{1 + sT_{ni}}{sT_{ni}} \tag{44}$$

With the parameters set to $k_{pi} = 100$ and $T_{ni} = 0.01$ a current control bandwidth of $\omega_{bi} = 300\,\text{Hz}$ and a phase margin of $60°$ can be reached.
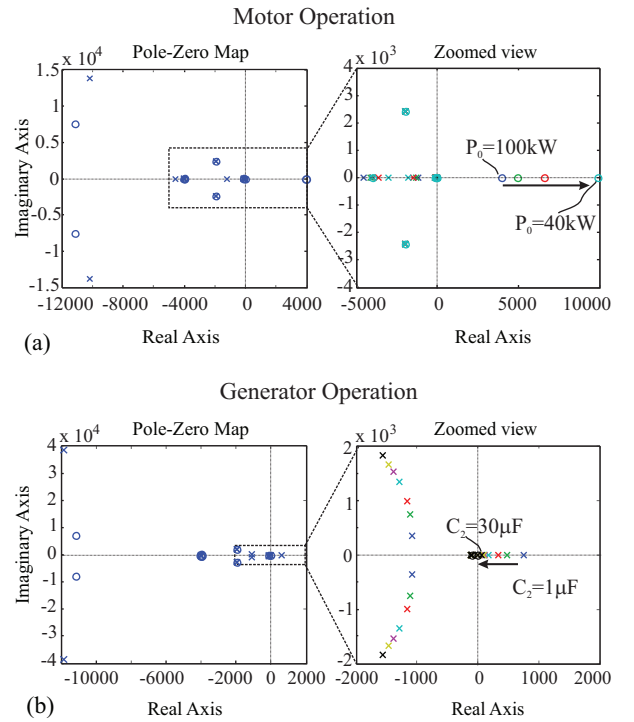


Fig. 26. Pole-zero map of the open-loop transfer function $G_{vTh2,Ruout}$ for (a) motor operation; the RHP zero moves farther to the right for lower output power $P_0$. (b) Generator operation; the zoomed view shows that the unstable RHP pole moves towards the origin for higher values of $C_2$.
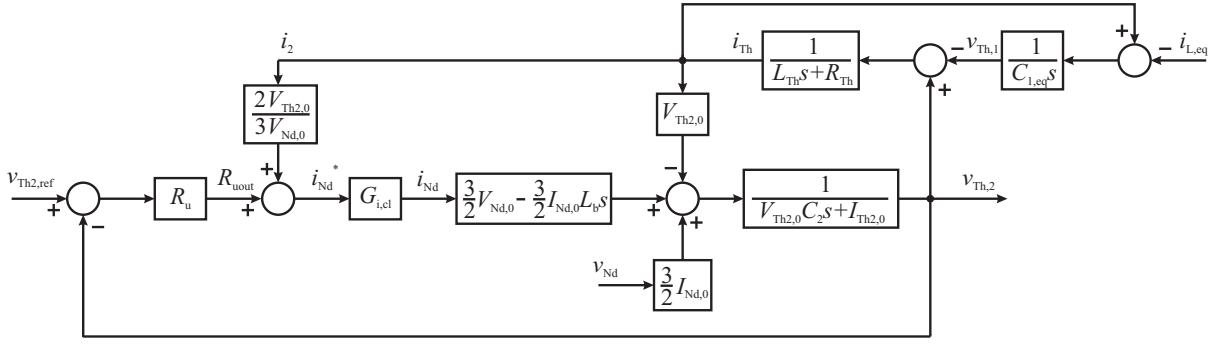
47

Fig. 27. Control block diagram.

Now, the dc-link voltage control has to be designed. Ideally there would be a voltage sensor at the dc–dc converter primary side but because of a missing real-time communication link with a small delay only the voltage $V_{Th,2}$ at the base station is sensed. For a better disturbance rejection additionally the current $I_{Th}$ flowing into the cable at the base station is measured and used as a feedforward expression in the final control loop which is depicted in Fig. 27.

The voltage controller $R_u$ regulates the dc-link voltage $V_{Th,2}$ at the base station. The open-loop transfer function for reference tracking $G_{vTh2,Ruout}$ can be derived from the block diagram by solving the corresponding loops. It is important that the feedforward path containing the measured current $I_{Th}$ is also included because it influences the transfer function and improves the achievable disturbance rejection.

$$G_{vTh2,Ruout} = \frac{v_{Th,2}}{R_{uout}}\bigg|_{v_{Nd}=0,\, i_{L,eq}=0} \tag{45}$$

The transfer function is dependent on the actual operating point for linearization.

$$V_{ud,0} = \hat{V}_N = 3.25\,\text{kV} \tag{46}$$

$$I_{Nd,0} = \frac{P_0}{3/2 \cdot V_{ud,0}} \tag{47}$$

$$V_{Th2,0} = 7.5\,\text{kV} \tag{48}$$

$$I_{2,0} = \frac{P_0}{V_{Th2,0}} \tag{49}$$

The main difference in the operating point is between motor ($P_0$ positive) and generator ($P_0$ negative) operation. In order to design a controller, both operating points have to be considered.

If the poles and zeros of the open-loop transfer function $G_{vTh2,Ruout}$ are examined, it can be seen that there is a RHP zero for motor operation [cf. Fig. 26(a)] and an unstable pole in the RHP for generator operation [cf. Fig. 26(b)]. This directly imposes some constraints on the voltage controller. In order to stabilize the system for generator operation, the controller bandwidth $\omega_{bu}$ has to be at least twice the RHP pole frequency $\omega_p$. Additionally, the RHP zero at $\omega_z$ gives an upper limit for the bandwidth in motor operation according to (51).

$$\omega_{bu} > 2 \cdot \omega_p \tag{50}$$

$$\omega_{bu} < \omega_z/2 \tag{51}$$

The RHP zero for motor operation is a well-known behavior of the ac–dc converter in rectifier operation. The location of the RHP zero is dependent on the value of the boost inductor $L_b$ and on the operating point defined by the nominal power $P_0$. If the power is decreased the zero moves to the right and has less influence [depicted

in the zoomed view of Fig. 26(b)]. The worst case operating point is for $P_0 = 100\,\text{kW}$ where the zero is located at $\omega_z = 4000\,\text{rad/s}$. Therefore, the maximum bandwidth of the voltage controller has to be lower than $2000\,\text{rad/s}$.

The location of the RHP pole in generator operation is dependent on the value of the capacitor $C_2$ at the base station [depicted in the zoomed view of Fig. 26(a)]. If it is increased, the RHP pole moves towards the origin. Because the achievable bandwidth of the voltage controller is limited, (50) gives directly a minimum for the capacitor $C_2$ to be installed at the base station. For $C_2 > 10\,\mu\text{F}$, the pole frequency is smaller than $180\,\text{rad/s}$, which can be stabilized with a controller bandwidth of $\omega_{bu} > 360\,\text{rad/s}$. In order to obtain a reasonable stability margin, the capacitor is finally chosen to be $C_2 = 20\,\mu\text{F}$.

Now the voltage controller gains will be determined for motor operation and then verified afterward for generator operation. In order to improve the disturbance rejection, a PI controller is enhanced with a lead-lag element to achieve a high crossover frequency with an appropriate phase margin.

$$G_{vTh2,cl} = \frac{v_{Th,2}}{v_{Th2,ref}} = \frac{R_u \cdot G_{vTh2,Ruout}}{1 + R_u \cdot G_{vTh2,Ruout}} \tag{52}$$

$$R_u = k_{pu}\frac{1+sT_{nu}}{sT_{nu}}\frac{1+sT_{lead}}{1+sT_{lp}} \tag{53}$$

With the parameters set to $k_{pu} = 0.02$ and $T_{nu} = 0.01$ a voltage regulation bandwidth of $\omega_{bu} = 900\,\text{rad/s}$ and a phase margin of $65°$ can be reached. The lead-lag element parameters are set to $T_{lead} =$
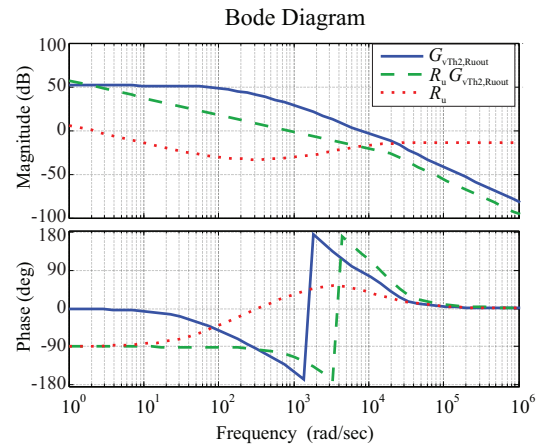


Fig. 28. Bode plot of plant $G_{vTh2,Ruout}$, controller $R_u$ and their open-loop interconnection $R_u\,G_{vTh2,Ruout}$ for motor operation $P_0 = 100\,\text{kW}$.
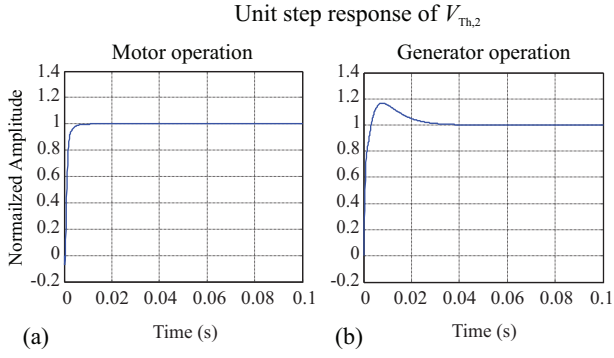
Fig. 29. Unit step response of closed-loop reference tracking transfer function $G_{vTh2,cl}$ for (a) motor operation and (b) generator operation.

0.001 and $T_{lp} = 1/10 T_{lead}$. The bode plot depicted in Fig. 28 shows the plant, the controller $R_u$ and the open-loop transfer function for motor operation. The bandwidth could not be increased much more because of the limitations imposed by the RHP zero (non-minimum phase behavior) and the time delay due to the PWM.

The performance for reference tracking and disturbance rejection can be checked by examining the step response of the corresponding transfer function. In Fig. 29(a) the response of the voltage $V_1$ on a unit step change is depicted for motor operation. The behavior is highly damped and no overshoot occurs. For generator operation, the same controller yields an overshoot of 20% which is not admissible [cf. Fig. 29(b)]. This problem could be resolved by introducing a further degree of freedom with a form filter for reference tracking.

$$G_{vTh2,cl} = \frac{v_{Th,2}}{v_{vTh2,ref}} = \frac{G_{rf} \cdot R_u \cdot G_{vTh2,Ruout}}{1 + R_u \cdot G_{vTh2,Ruout}} \tag{54}$$

$$G_{rf} = \frac{1}{1 + sT_{rf}} \tag{55}$$

With $T_{rf} = 0.01$ the step response is sufficiently damped and the overshoot is completely removed also for generator operation. Naturally, the rise time is reduced but this can be accepted because a fast reference tracking is not a main control goal.

Now the influence of load changes on the bus voltages at the base station and at the dc–dc converter can be examined. The closed-loop transfer functions related to disturbance rejection can be found by solving the corresponding loops.

$$G_{vTh2,iL} = \frac{v_{Th,2}}{i_{L,eq}} \bigg|_{v_{Nd}=0, v_{Th2,ref}=0} \tag{56}$$

$$G_{vTh1,iL} = \frac{v_{Th,1}}{i_{L,eq}} \bigg|_{v_{Nd}=0, v_{Th2,ref}=0} \tag{57}$$

The responses of the cable voltages $V_{Th,2}$ and $V_{Th,1}$ on a step change of the load current for motor and generator operation are depicted in Fig. 30(a) and Fig. 30(b), respectively. The load change considered for motor operation is a load drop from nominal power $P = 100\,\text{kW}$ to zero. The MV cable voltage rises up to 7.75 kV what corresponds to a deviation of 3.3% from the nominal voltage. It is still within the allowed voltage band. A complete power reversal from motor to generator operation (from $P = 100\,\text{kW}$ to $P = -100\,\text{kW}$) would exactly hit the maximum cable voltage of 8 kV and could be accepted. Such a reversal is unlikely to happen as an external disturbance. If it is triggered by control commands a certain power slew rate could be implemented to reduce the cable overvoltage. The difference between the voltage at the base station $V_{Th,2}$ and at the kite $V_{Th,1}$ is small
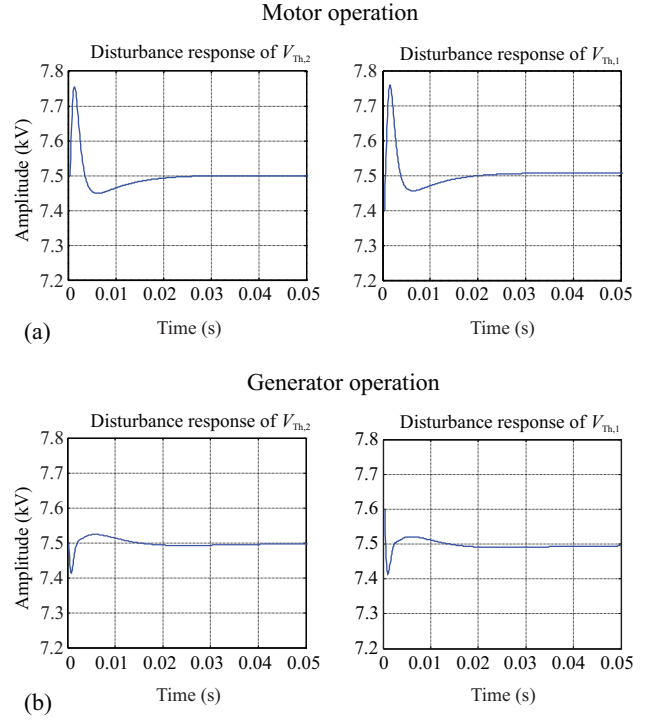


Fig. 30. (a) Response of $V_{Th,2}$ and $V_{Th,1}$ on a step in $i_{L,eq}$ from 13.3 A to 0 A corresponding to a step change of $P = 100\,\text{kW}$ to $P = 0\,\text{kW}$ in motor operation; (b) response of $V_{Th,2}$ and $V_{Th,1}$ on a step in $i_{L,eq}$ from $-13.3\,\text{A}$ to 0 A corresponding to a step change of $P = -100\,\text{kW}$ to $P = 0\,\text{kW}$ in generator operation.

except of a certain offset due to the voltage drop on the cable series resistance.

The load change considered for generator operation is a complete energy generation stop corresponding to a change in the transmitted power from $-100 \ldots 0\,\text{kW}$. The voltage $V_{Th,2}$ is tightly regulated and shows a maximum deviation of only 1.5% from the nominal value. Again, the difference of $V_{Th,1}$ compared to $V_{Th,2}$ is mainly due to the voltage drop over the series resistance of the cable. The designed controller is able to keep the bus voltage in the desired band even for drastic load changes during generator operation. Correspondingly, also the voltage on the low-voltage side of the dc–dc converter will stay within its limits, which can be seen if the voltage transfer ratio $n_t$ is considered.

## IV. CONCLUSIONS

As shown in the present work, AWTs represent a concept that offers numerous technical challenges but which, in the end, is technically feasible on the basis of the latest technology. For a 100 kW AWT system with 8 turbines and a total shaft power of 100 kW, there results an overall weight of the power electronics converters and the generators/motors on the aerofoil of approximately 70 kg and a tether's weight of 320 kg at an efficiency from the turbine shaft to the ground station of 90%; the power converters and the generators/motors share 20% of the total weight of the electric system including the tether. Thus, future research may address a further weight reduction of the tether. The power electronics system, despite the relatively small capacitive energy storage (weight limitation) and the long MV connection to the ground, is readily manageable from the control point of view. The suggested control structure thus provides a basis for the design of an overriding control, i.e. in

particular an on-line optimization of the flight trajectory for maximum power gain, whereby the handling of highly variable wind conditions, and automatic takeoff and landing are of particular importance. Furthermore, apart from regular operation, failures such as loss of a generator/motor unit on the airborne system part or a failure of the grid must be considered.

It is intended to answer these questions in the course of further research on the basis of a complete dynamic model of the system, i.e. of the electrical part (generator, power electronics and cooling arrangement), the aerodynamic part including the tether, and the grid. Here also, for example, the thermo-mechanical loading of the power semiconductor modules caused by the variations of the power flow, in seconds, along the flight trajectory and hence also of the power semiconductor junction temperatures will be analyzed and the mechanical loading of the tether (material fatigue) investigated. Certainty regarding the actual practical feasibility of the concept will finally be brought by the long-term test of a demonstrator. Here questions of lightning protection or acoustic noise emissions can also be examined. After overcoming all technical challenges, there remains the scaling-up of the concept to the megawatt range and a final economic evaluation. This appears to be very promising because of the considerably lower consumption of resources compared to conventional wind power exploitation, provided the technology can be reliably mastered.

APPENDIX

*A. Basics of Aerodynamics of Conventional Wind Turbines and Power Kites*

The following is intended to briefly illustrate the fundamental mathematical relationships for the calculation of a wind turbine's rotor blade swept area $A_T$ (Section A1) and the power generation of rotor blades (Section A2) and power kites (Section A3) in greatly simplified form. This conveys on the one hand an insight into the physical relationships and shows on the other hand, taking a $100\,\text{kW}$ system as an example, that the surface area of a kite intended for an Airborne Wind Turbine (AWT) can be approximately the same as the surface area of the rotor blades of a conventional two-blade wind turbine.

*1) Conventional Wind Turbines:* The kinetic energy of an axial air flow is transformed into torque-forming tangential force through the rotor blades of a windmill. According to Lanchester and Betz, the calculation of the maximum achievable power for a given rotor blade swept area $A_T$ can be replaced by a partially air-permeable actuator disc [1], [31] and the power flow can be considered in a tubular air flow as shown in Fig. 31. The pressure in front of the disc will increase in relation to the ambient pressure, i.e. the kinetic energy of the air will be reduced, respectively the flow cross-section widened and a force applied to the turbine disc. The removal of energy from the disc causes a steep reduction of the pressure. At a later stage, due to the further reduction of the air speed, the air flow once again reaches the ambient pressure and finally through the absorption of the kinetic energy from the surrounding air again attains the original wind speed $v_W$. In contrast to the pressure, the speed, assuming constant air density on the basis of the same mass flow per second through all cross-sections,

$$\dot{m} = \rho A_W v_W = \rho A_T v_T = \rho A_E v_E \,, \qquad (58)$$

shows a continuous development. This provokes the question, which terminal velocity of the air $v_E$ results in maximum turbine power. In this connection it is worth noting that $v_E = 0$ is not an optimum
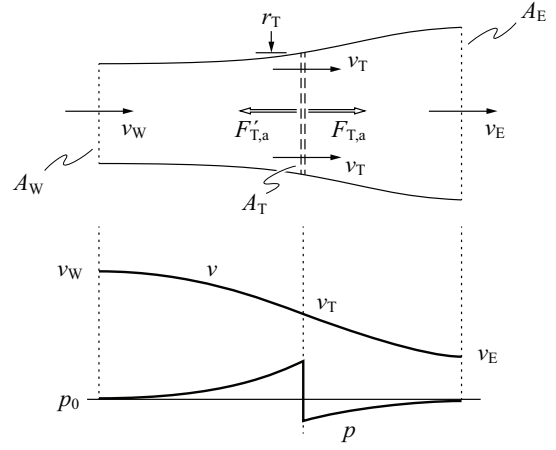


Fig. 31. Setup considered for the derivation of Betz' Law (airflow tube with turbine replaced by actuator disk); wind speed and pressure profile.

value, as then the air behind the wind turbine cannot leak away, i.e. the flow of additional air would be impaired.

The force acting on the turbine disc results from the conservation of momentum

$$F_{T,a} = \dot{m}\,(v_W - v_E) \qquad (59)$$

and thereby the power generated from the airflow according to the principle of virtual displacement is

$$P_T = F_{T,a} v_T = \dot{m}\,(v_W - v_E)\,v_T \,. \qquad (60)$$

Furthermore, we have for the power according to the principle of conservation of energy

$$P_T = \frac{1}{2}\dot{m}\,\left(v_W^2 - v_E^2\right) \,. \qquad (61)$$

For this reason follows by a combination of (60) and (61)

$$v_T = \frac{1}{2}\,(v_W + v_E) \,, \qquad (62)$$

i.e. the air speed on the disc is the same as the average of the initial and terminal velocities. The optimal speed $v_E$ can now by use of (58) in (61)

$$P_T = \frac{1}{2}\rho A_T v_T \left(v_W^2 - v_E^2\right) = \frac{1}{4}\rho A_T \left(v_W + v_E\right)\left(v_W^2 - v_E^2\right) \qquad (63)$$

be calculated in the form of a simple extreme value problem

$$\frac{dP_T}{dt} = 0 \longrightarrow v_{E,i} = \frac{1}{3}v_W \,. \qquad (64)$$

This results in a maximum achievable power from the wind (Betz Limit, indicated by an index i)

$$P_{T,i} = c_{P,i}\frac{1}{2}\rho A_T v_W^3 = c_{P,i} P_W \quad \text{with} \quad c_{P,i} = \frac{16}{27} \approx 0.59 \,, \qquad (65)$$

whereby $c_{P,i}$ denotes the power coefficient for the Betz Limit. Accordingly, $59\%$ of the power $P_W$ of undisturbed wind flowing through the area $A_T$ with speed $v_W$ can be used.

The power that can be generated increases only linear with the area $A_T$, however with the third power of the wind speed $v_W$; therefore, an increase of $v_W$ by only $25\%$ already results in a doubling of the turbine output.

Combining (58), (59) and (64) we now have for the axial force $F_{T,i,a}$ acting on the tower of a windmill

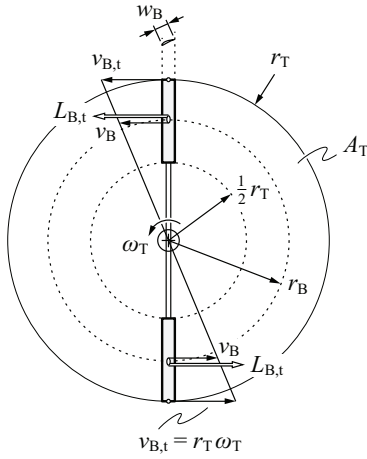$$F_{T,a,i} = \rho A_T \frac{4}{9}v_W^2 = \frac{3}{2}\frac{P_{T,i}}{v_W} \qquad (66)$$

50

Fig. 32. Turbine swept area and blade area.



Fig. 33. Velocity components and forces acting on the blade of a CWT.

i.e. accordingly

$$F_{T,a,i}\, v_W = \frac{3}{2} P_{T,i} \ . \tag{67}$$

In simple terms only $2/3$ of the energy that would be necessary to push the turbine disc with a speed of $-v_W$ against still air can be gained. This observation is of importance for the calculation of the AWT in Section A3.

The turbine area $A_T$ is determined by

$$A_T = r_T^2 \pi \ . \tag{68}$$

In the case of a real turbine, however, only a part of the entire area $A_T$ effectively generates power. Here, for an approximate estimate, it can be considered that within an inner circle having the radius $r_T/2$, no power can be generated, i.e. the actual turbine area is only $3/4 A_T$. The turbine output then is

$$P_T = \frac{3}{4} P_{T,i} = \frac{2}{9} \rho A_T v_W^3 \ . \tag{69}$$

This represents using $44\%$ of $P_W$ [cf. (65)] and coincides with practically achieved values. The turbine area necessary to generate power $P_G$ is thus

$$A_T = \frac{P_G}{\frac{2}{9} \rho v_W^3} \ . \tag{70}$$

In axial direction the resultant force is

$$F_{T,a} = \frac{3}{4} F_{T,a,i} + c_W \frac{1}{2} \rho \frac{A_T}{4} v_W^2 = \left(1 + \frac{3}{8} c_W\right) \frac{3}{2} \frac{P_T}{v_W} \approx \frac{3}{2} \frac{P_T}{v_W} \ , \tag{71}$$

whereby the aerodynamic resistance caused by the inner, non-active part of the turbine is considered. Assuming an aerodynamically-favorable design of the non-active part ($c_W = 0.2$ typ.) this portion can, however, be neglected in respect of the axial force resulting from the turbine effect.

*2) Geometrical Dimensions of the Rotor Blades of CWTs:* The greatly simplified arrangement of a twin blade turbine with a concentrated force acting on a mean radius $r_B$ shown in Fig. 32 is used to calculate the blade surface $A_B$ and/or the geometrical dimensions of the rotor blades. Furthermore, the analysis of the air flow will be limited to this radius. In contrast, a more accurate calculation would require a dissection of the rotor blades into a large number of small radial sections [32].

It should be noted that twin blade turbines are used industrially up to about $100\,\text{kW}$ (the same as the rated power of the AWT system
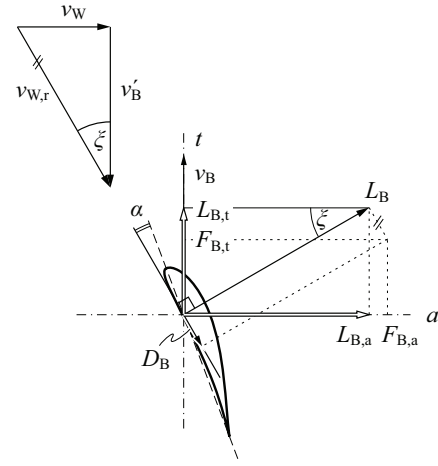
considered in this paper). For higher power levels the propellers are equipped with three rotor blades which provide a better balance of the masses, a more uniform torque generation (lee of the tower) and reduced rotational speed.

An important aspect when dimensioning wind turbines is the tip speed ratio

$$\lambda_T = \frac{r_T \omega_T}{v_W} \tag{72}$$

that is selected, based on experience from turbine construction [33] as

$$\lambda_{T,opt} \approx \sqrt{\frac{80}{z_B}} \tag{73}$$

($z_B$ indicates the number of rotor blades). It is clear in the aim for an optimal tip speed ratio that for too low rotational speed $\omega_T$ and/or tip speed of the turbine rotor blades, the area $A_T$ is passed over too slowly, in other words the wind can pass through without hindrance and/or without extraction of a large amount of energy. At too high a speed the rotor blades can, in the limiting case, block the air stream which once again results in a low energy extraction. Furthermore, at too high $\omega_T$ a rotating rotor blade reaches the turbulent air left behind the preceding blade resulting in high aerodynamic resistance and/or losses.

For the conversion of the wind energy advantageously the lift $L_B$ acting orthogonally to the wind speed $v_{W,r}$ observed from the rotor blade, is employed (cf. Fig. 33). The lift generated depends essentially on the direction of the relative wind to the rotor blade chord line, i.e. the angle of attack $\alpha$. Increasing $\alpha$ results in increased lift $L_B$ until finally a strong increase in drag and last of all turbulent air currents result (pp. 60–61 in [1]). Due to the increasing peripheral speed $v_B$, caused by the increasing radius, the blade pitch angle is changed over the radius for real turbines.

The effective air flow results in a lift $L_B$ and drag $D_B$ acting on the rotor blade

$$L_B = c_{LB} \frac{1}{2} \rho A_B v_{W,r}^2 \quad D_B = c_{DB} \frac{1}{2} \rho A_B v_{W,r}^2 \ , \tag{74}$$

with $c_{LB} = 1 \ldots 1.5$ and $c_{DB} = 0.05 \ldots 0.1$ (lift-to-drag ratio $c_{LB}/c_{DB} = 15$ typ.) for an appropriately shaped blade profile and an optimal angle of attack. Accordingly, the drag effect of $D_B$ can be disregarded in the following.
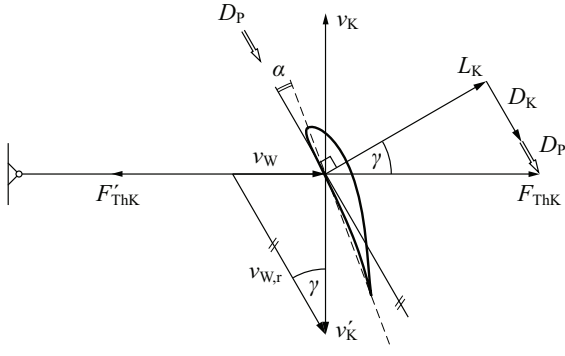
51

Fig. 34. Velocity components and forces acting on the power kite of an AWT (turbines not shown, cf. Fig. 35).



Fig. 35. Schematic representation of an AWT section (power kite wing carrying wind turbines, cf. Fig. 2).

The effective wind speed follows with the tangentially directed rotor blade speed

$$v_B = \frac{3}{4} r_T \omega_T = \frac{3}{4} \lambda_T v_W \qquad (75)$$

as

$$v_{W,r} = \sqrt{v_W^2 + v_B^2} = v_W \sqrt{1 + \frac{9}{16} \lambda_T^2} \ . \qquad (76)$$

The force component acting in the blade's direction of rotation is thus

$$L_{B,t} = L_B \sin \xi = L_B \frac{v_W}{v_{W,r}} = c_L \frac{1}{2} \rho A_B v_W^2 \sqrt{1 + \frac{9}{16} \lambda_T^2} \ , \qquad (77)$$

and we have with reference to Fig. 33

$$\frac{L_{B,t}}{L_{B,a}} = \frac{v_W}{v_B} \longrightarrow L_{B,t} v_B = L_{B,a} v_W \ . \qquad (78)$$

This well shows the power conversion by the rotor blade from the axial wind direction into a torque-forming tangential component.

The wind speed on the rotor blades was assumed to be $v_W$ for the previous calculations. However, as can be derived from (65), only a wind speed of $2/3\, v_W$ reaches the turbine disc [cf. (62) and (64)]. It is thus necessary to reduce the tangential force, calculated according to (77), to $2/3\, L_{B,t}$, for the torque generation. As a result it will be clear that also the full axial force $F_{B,a}$ according to (71) corresponds with $3/2\, P_T$ and not directly with $P_T$.

In summary, we have for an output power $P_G$ (referenced to the turbine shaft) to be generated by the turbine,

$$P_G = z_B \frac{2}{3} L_{B,t} v_B = z_B \frac{1}{4} c_L \rho A_B v_W^3 \lambda_T \sqrt{1 + \frac{9}{16} \lambda_T^2} \qquad (79)$$

($z_B$ denominates the number of rotor blades), which allows to calculate the required rotor blade area $A_B$ and/or the rotor blade width

$$w_B = \frac{A_B}{\frac{1}{2} r_T} \qquad (80)$$

as $r_T$ is determined by (68) and (69).

*3) Crosswind Power Kite Modeling:* A crosswind kite moves transversal to the wind in the same manner as the rotor blade of a windmill, i.e. the aerodynamic area $A_K$ converts wind energy to move the kite against the aerodynamic resistance. It is assumed that the kite retaining cable lies parallel to the wind, whereby the motion is orthogonal to $v_W$ (cf. Fig. 34) and $v_K$ shows a constant value, i.e. no acceleration forces occur, for the sake of simplicity in the following observations. In reality, this situation is given only in sections of the kite figure-of-eight flight trajectory.
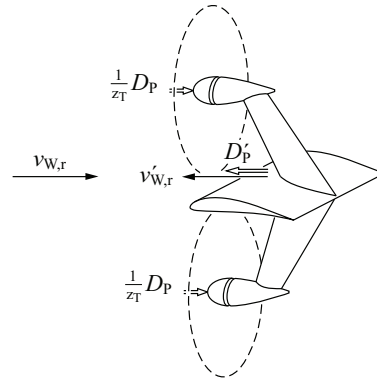
For the lift $L_K$ and drag $D_K$ acting upon the kite we have

$$L_K = c_{LK} \frac{1}{2} \rho A_K v_{W,r}^2 \quad D_K = c_{DK} \frac{1}{2} \rho A_K v_{W,r}^2 \ . \qquad (81)$$

In case wind turbines are mounted on the kite according to [2] (cf. Fig. 35), i.e. an Airborne Wind Turbine (AWT) is created, a counteracting force takes effect, in addition to the aerodynamic drag, which reflects the energy generated by the turbine for a wind speed $v_{W,r}$. In addition to $D_L$ and $D_P$ the lift must also support the weight $G_K$ of the kite itself as well as that of the retaining cable (tether) $G_{Th}$ and causes a tensile loading of the tether. Within the terms of a basic overview, $G_K$ and $G_{Th}$ will not be considered here [2]. Therefore, the forces $L_K$, $D_K$ and $D_P$ combine to a resulting force acting in the direction of the tether.

The aerodynamic quality of an aerofoil respectively a kite is determined by the lift-to-drag ratio which is itself dependent on the angle of attack $\alpha$ (cf. Section A2)

$$k_{LD} = \frac{L_K}{D_K} = \frac{c_{LK}}{c_{DK}} \qquad (82)$$

and typically has values of $k_{LD} = 20 \dots 30$. We will denote the relationship of the energy-generating force $D_P$ to the aerodynamic drag $D_K$ with

$$k_D = \frac{D_P}{D_K} \ . \qquad (83)$$

Based on the speed diagram (cf. Fig. 34) we have

$$\frac{v_W}{v_{W,r}} = \sin \gamma = \frac{\tan \gamma}{\sqrt{1 + \tan^2 \gamma}} \qquad (84)$$

with

$$\tan \gamma = \frac{D_K + D_P}{L_K} = \frac{(1 + k_D)}{k_{LD}} \qquad (85)$$

and $v_{W,r}$ results as

$$v_{W,r} = v_W \frac{\sqrt{k_{LD}^2 + (k_D + 1)^2}}{(k_D + 1)} \approx v_W \frac{k_{LD}}{(k_D + 1)} \qquad (86)$$

($k_{LD} \gg 1$), i.e. the flying speed of the kite is several times higher than the actual wind speed $v_W$. The power extractable by the kite is

$$P_K = v_{W,r} D_P = v_{W,r} k_D \frac{L_K}{k_{LD}} = c_{LK} \frac{1}{2} \rho A_K \frac{k_D}{k_{LD}} v_{W,r}^3$$
$$\approx c_{LK} \frac{1}{2} \rho A_K v_W^3 k_{LD}^2 \frac{k_D}{(k_D + 1)^3} \ . \qquad (87)$$
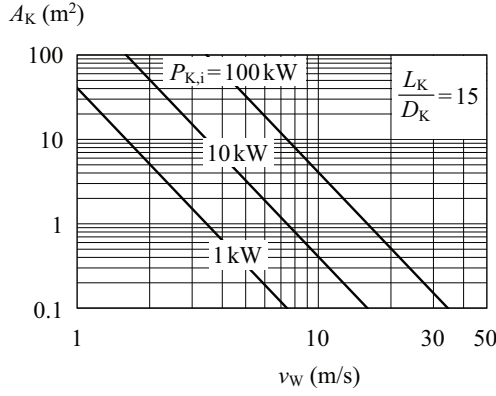
$A_K$ (m²)

Fig. 36. Dependency of the power kite output power on the effective air velocity $v_{W,r}$ and the kite area $A_K$ under the assumption of optimal selection of $D_P$, i.e. $D_P = D_{P,i} = 1/2 D_K$; cf. (88).

Accordingly, the power generation for given aerodynamic properties $k_{LD}$ and $c_{LK}$ can be maximized by proper choice of $k_D$, i.e.

$$\frac{\mathrm{d}P_K}{\mathrm{d}k_D} = 0 \longrightarrow k_{D,i} = \frac{1}{2}, \quad D_{P,i} = \frac{1}{2}D_K . \tag{88}$$

Eq. (88) has to be interpreted such, that for small values $k_D$ or $D_P$, despite a high speed $v_K$, a small product value (87) results. In contrast, a considerable reduction of $v_K$ results from a high $D_P$ and with this once again a low power generation. By the use of (88) in (87) we have

$$P_{K,i} \approx \frac{4}{27}c_{LK}k_{LD}^2 \frac{1}{2}\rho A_K v_W^3 = c_{PK,i}\frac{1}{2}\rho A_K v_W^3 . \tag{89}$$

Thereby, it becomes clear that the kite's coefficient of performance $c_{PK,i}$ is considerably higher than that of a CWT [cf. $c_{P,i}$, (65)], i.e. in order to generate a predefined power value, the kite surface $A_K$ (cf. Fig. 36) can be considerably smaller than the swept area $A_T$ of an ground-based turbine; e.g. for $c_{LK} = 1.2$ and $k_{LD} = 20$ we have $c_{PK,i}/c_{P,i} = 120$ clearly showing the kite's relationship with the rotor blades of the CWT mentioned above. It is important to point out that based on (88) one should not assume that in order to generate more power a greater kite wind resistance (drag) $D_K$ is desirable. On the contrary, as shown by (89), the maximum power $P_{K,i}$ increases with increasing $k_{LD}$, i.e. reducing $D_K$. However, in any case twice the generated power is lost to the aerodynamic drag $D_K$ also in the optimal case.

At optimal $k_D$, i.e. $k_{D,i} = 1/2$, the wind speed seen from the kite (according to Fig. 35 wind speed $v_{W,r,i}$ for large $k_{LD}$ is approximately the same as the flying speed of the kite $v_K$ measured in a fixed coordinate system) is

$$v_{W,r,i} \approx v_W \frac{k_{LD}}{(k_D + 1)} = \frac{2}{3}k_{LD}v_W . \tag{90}$$

This is $2/3$ of the speed of a kite which is not retarded by a turbine counteracting force $D_P$, but nevertheless still several times higher than the wind speed $v_W$, advantageously resulting in a very small swept area $A_{TK}$ (cf. Section A4) requirement for the kite's turbines.

*4) Power Kite Area and Turbines:* Finally the swept area $A_{TK}$ of the wind turbines mounted on the kite and their rotational speed $\omega_{TK}$, and the rotor blade area $A_{BK}$ must be calculated, whereby it will again be assumed that a twin blade turbine is used.

Dimensioning of the kite for optimal operation results in a very high speed $v_{W,r,i}$ (in the case of a kite turbine $v_{W,r}$ replaces the

wind speed $v_W$ applicable to a ground-based turbine) and thus, according (70), a very small turbine area $A_{TK}$

$$A_{TK} = \frac{P_G}{z_T \frac{2}{9}\rho v_{W,r}^3} = r_{TK}^2 \pi \tag{91}$$

or short rotor blades $r_{TK}$ ($P_G$ is the total power to be generated, $z_T$ the number of kite mounted turbines, cf. Fig. 3). Furthermore, as a result of the tip speed ratio resulting from the number of rotor blades according to (73)

$$\lambda_{TK} = \frac{r_{TK}\omega_{TK}}{v_{W,r}} , \tag{92}$$

a very high angular frequency $\omega_{TK}$ of the turbine will result.

It is therefore advantageous to take an opposite approach and to choose sufficiently long rotor blades $r_{TK}$ respectively a sufficiently large swept area $A_{TK}$ (sufficiently larger than the outer radius of the generator positioned behind the turbine). The necessary wind speed $v_{W,r}$ can then be calculated by use of (69)

$$v_{W,r}^3 = \frac{P_G}{\frac{2}{9}\rho z_T A_{TK}} . \tag{93}$$

The rotational speed $\omega_{TK}$ of the turbine then results from the choice of $\lambda_{TK}$ (92). The area $A_{BK}$ and width $w_{BK}$ of the kite turbine rotor blades can be calculated according to Section A2.

It should be pointed out that in general the optimum application of the kite to generate power according (89) cannot be achieved, hence a larger kite surface area $A_K$ than defined by (92), is required. In order to calculate $A_K$ it can be assumed that the force acting on the kite due to the mounted turbines $z_T$ is

$$F_{TK,a} \approx z_T \frac{3}{2}\frac{P_{TK}}{v_{W,r}} = \frac{3}{2}\frac{P_G}{v_{W,r}} \tag{94}$$

[compare comment to (67)]. This force is directly the same as $D_P$,

$$D_P = F_{TK,a} \approx \frac{3}{2}\frac{P_G}{v_{W,r}} \tag{95}$$

whereby $D_P$ is specified; furthermore $v_{W,r}$ is known from (93). Thus the kite's output power is

$$P_K = v_{W,r}D_P = \frac{3}{2}P_G \tag{96}$$

i.e. a power of $3/2$ of the total turbine output power has to be supplied by the kite. By rearranging (86) we obtain

$$k_D = \left(\frac{v_W}{v_{W,r}}k_{LD} - 1\right) \tag{97}$$

and thus by use of (87)

$$P_G \approx c_{LK}\frac{1}{3}\rho A_K \left(\frac{v_W}{v_{W,r}} - \frac{1}{k_{LD}}\right)v_{W,r}^3 \tag{98}$$

from which the necessary kite area

$$A_K \approx \frac{P_G}{c_{LK}\frac{1}{3}\rho \left(\frac{v_W}{v_{W,r}} - \frac{1}{k_{LD}}\right)v_{W,r}^3} \tag{99}$$

immediately results.

*5) Numerical Results:* In this section a calculation example of a conventional ground-based wind turbine and an airborne crosswind power kite with $z_T = 8$ turbines is presented based on the equations derived in this appendix. Both wind turbine systems are designed for a total mechanical shaft power $P_G = 100\,\mathrm{kW}$, a wind speed $v_W = 10\,\mathrm{m/s}$, and a rotor blade number $z_B = 2$ (two-blade rotor). The aim is to briefly investigate and compare the physical dimensions and properties of both systems.

Firstly, the conventional wind turbine is considered. According to (70), the necessary swept area of the rotor equals to

$$A_\text{T} = \frac{P_\text{G}}{\frac{2}{9}\rho v_\text{W}^3} = 367.3\,\text{m}^2 \,, \qquad (100)$$

leading to a rotor radius

$$r_\text{T} = \sqrt{\frac{A_\text{T}}{\pi}} = 10.8\,\text{m} \,. \qquad (101)$$

The resultant angular speed $\omega_\text{T}$, assuming an optimal tip speed ratio can be determined by combination of (72) and (73) and is given by

$$\omega_\text{T} = \frac{v_\text{W}}{r_\text{T}}\sqrt{\frac{80}{z_\text{B}}} = 5.8\,\text{rad/s}^{-1} \,. \qquad (102)$$

This corresponds to a rotational speed of 56 rpm. The required blade area can then be determined by solving (79) for $A_\text{B}$, which leads to

$$A_\text{B} = \frac{4 P_\text{G}}{z_\text{B}\rho v_\text{W}^3 \lambda_\text{T,opt}\sqrt{1 + \frac{9}{16}\lambda_\text{T,opt}^2}} = 4.4\,\text{m}^2 \qquad (103)$$

for a lift coefficient $c_\text{L} = 1.2$ and an optimal tip speed ratio $\lambda_\text{T,opt}$ according to (73). Ultimately, (80) allows for the calculation of the required rotor blade width.

$$w_\text{B} = \frac{2 A_\text{B}}{r_\text{T}} = 0.8\,\text{m} \qquad (104)$$

Next, the characteristic quantities of the power kite are determined for a lift coefficient $c_\text{LK} = 1.2$, a lift-to-drag ratio $k_\text{LD} = 25$, and a rotor radius $r_\text{TK} = 0.625\,\text{m}$ (equals to a diameter of 1.25 m). The rotational speed of the generator/motor is assumed with 2000 rpm at generator operation and 3000 rpm at motor operation.

The required relative wind speed $v_\text{W,r}$, seen by the kite wind turbines, can be calculated by (93)

$$v_\text{W,r} = \sqrt[3]{\frac{P_\text{G}}{\frac{2}{9}\rho z_\text{T} A_\text{TK}}} = 33.4\,\text{m/s} \,, \qquad (105)$$

which corresponds to a speed of $120\,\text{km/h} \approx 65\,\text{kts}$. The necessary kite (wing) area can then immediately be obtained from (99)

$$A_\text{K} \approx \frac{P_\text{G}}{c_\text{LK}\frac{1}{3}\rho\left(\frac{v_\text{W}}{v_\text{W,r}} - \frac{1}{k_\text{LD}}\right) v_\text{W,r}^3} = 21.1\,\text{m}^2 \,. \qquad (106)$$

Finally, the resulting tip speed ratio has to be determined for generator operation ($\lambda_\text{TK,g}$) and for motor operation ($\lambda_\text{TK,m}$) using (92) to verify the turbine rotor design.

$$\lambda_\text{TK,g} = \frac{r_\text{TK}\omega_\text{TK,g}}{v_\text{W,r}} = 3.9 \qquad (107)$$

$$\lambda_\text{TK,m} = \frac{r_\text{TK}\omega_\text{TK,m}}{v_\text{W,r}} = 5.9 \qquad (108)$$

For motor operation, the tip speed ratio is close to the optimal value ($\approx 6.32$) for a two-blade rotor as desired.

By considering the rotor radius $r_\text{T}$ and $r_\text{TK}$, it can be shown that the total swept area of the turbines on the power kite, operating at 2000 rpm, is approximately 37 times smaller than the swept area of the ground-based wind turbine, operating at 56 rpm.

*6) List of Symbols:* The acronyms and variables utilized for the aerodynamic calculations in the appendix are listed below. The term "turbine" refers to wind turbines if not differently specified.

| | |
|---|---|
| AWT | Airborne wind turbine |
| CWT | Conventional (ground-based) wind turbine |
| $A_\text{B}$ | Rotor blade area |

| | |
|---|---|
| $A_\text{E}$ | Exit area of the airflow tube |
| $A_\text{K}$ | Kite (wing) area |
| $A_\text{T}$ | Swept area by the rotor of the turbine |
| $A_\text{TK}$ | Swept area by the rotor of the turbine on the kite |
| $F_\text{T,a}$ | Axial force acting on the turbine |
| $F_\text{T,t}$ | Tangential force acting on the turbine |
| $F_\text{TK,a}$ | Axial force acting on the turbine of the kite |
| $D_\text{B}$ | Drag of the rotor blade |
| $D_\text{P}$ | Power generating drag of the kite |
| $D_\text{K}$ | Aerodynamic drag of the kite |
| $L_\text{B}$ | Lift of the rotor blade |
| $L_\text{B,a}$ | Axial lift acting on the rotor blade |
| $L_\text{B,t}$ | Tangential lift acting on the rotor blade |
| $L_\text{K}$ | Lift of the kite |
| $P_\text{G}$ | Total shaft power of the wind or kite turbine system |
| $P_\text{K}$ | Extractable power by the kite (wing) |
| $P_\text{K,i}$ | Maximum extractable power by the kite (wing) for ideal selection of $k_\text{D} = k_\text{D,i} = 0.5$ |
| $P_\text{T}$ | Power of the turbine |
| $P_\text{T,i}$ | Maximum achievable power of the turbine for $c_\text{P} = c_\text{P,i}$ (Betz Limit) |
| $P_\text{W}$ | Power of the undisturbed wind |
| $c_\text{D}$ | Drag coefficient |
| $c_\text{DK}$ | Drag coefficient of the kite |
| $c_\text{L}$ | Lift coefficient |
| $c_\text{LB}$ | Lift coefficient of the rotor blade |
| $c_\text{LK}$ | Lift coefficient of the kite |
| $c_\text{P}$ | Power coefficient of the turbine |
| $c_\text{P,i}$ | Ideal power coefficient of the turbine ($c_\text{P,i} \approx 0.59$) |
| $c_\text{PK}$ | Power coefficient of the kite |
| $c_\text{PK,i}$ | Ideal power coefficient of the kite ($k_\text{D,i} = 0.5$) |
| $c_\text{W}$ | Aerodynamic resistance coefficient |
| $k_\text{D}$ | Ratio of the power generating drag to the aerodynamic drag of the kite |
| $k_\text{D,i}$ | Ideal ratio of the power generating drag to the aerodynamic drag of the kite ($k_\text{D,i} = 0.5$) |
| $k_\text{LD}$ | Lift-to-drag ratio |
| $m$ | Mass of the air |
| $r_\text{T}$ | Rotor radius of the turbine |
| $r_\text{TK}$ | Rotor radius of the turbine on the kite |
| $v_\text{B}$ | Velocity of the rotor blade |
| $v_\text{E}$ | Exit air velocity of the airflow tube |
| $v_\text{E,i}$ | Ideal exit air velocity of the airflow tube ($v_\text{E,i} = 1/3 v_\text{W}$) |
| $v_\text{K}$ | Kite velocity (speed) |
| $v_\text{T}$ | Air velocity at the turbine of the airflow tube |
| $v_\text{W}$ | Wind velocity (speed) |
| $v_\text{W,r}$ | Relative wind velocity acting on the rotor blade or the kite |
| $w_\text{B}$ | Rotor blade width |
| $z_\text{B}$ | Number of rotor blades |
| $z_\text{T}$ | Number of turbines on the kite |
| $\gamma$ | Angle between $v_\text{K}$ and $v_\text{W,r}$; not to be confused with the power-to-weight or more precisely the power-to-mass ratio |
| $\lambda_\text{T}$ | Tip speed ratio of the turbine |
| $\lambda_\text{TK}$ | Tip speed ratio of the turbine on the kite |
| $\lambda_\text{T,opt}$ | Optimal tip speed ratio of the turbine |
| $\rho$ | Density of the air ($\rho = 1.225\,\text{kg}/m^3$ at $15°\text{C}$) |
| $\xi$ | Angle between $v_\text{B}$ and $v_\text{W,r}$ |
| $\omega_\text{T}$ | Angular frequency of the turbine |
| $\omega_\text{TK}$ | Angular frequency of the turbine on the kite |

## REFERENCES

[1] A. Betz, *Windenergie und ihre Ausnutzung in Windmühlen (in German)*. Bandenhoeck & Ruprecht: Göttingen, 1926.

[2] M. L. Loyd, "Crosswind kite power," *Journal of Energy*, vol. 4, no. 3, pp. 106–111, May/June 1980.

[3] SwissKitePower. Accessed: April 2011. [Online]. Available: http://www.swisskitepower.ch/

[4] Kite Gen. Accessed: April 2011. [Online]. Available: http://kitegen.com/

[5] L. Fagiano, M. Milanese, and D. Piga, "High altitude wind power generation," *IEEE Trans. Energy Convers.*, vol. 25, no. 1, pp. 168–180, Mar. 2010.

[6] W. J. Ockels, B. Lansdorp, J. Breukels, and G. Spierenburg, "The laddermill: work in progress," in *Proc. European Wind Energy Conference*, London, UK, Nov. 22–25, 2004, pp. 1–7.

[7] M. Diehl and B. Houska, "Windenergienutzung mit schnell fliegenden Flugdrachen: Eine Herausforderung für die Optimierung und Regelung (in German) – Wind power via fast flying kites: A challenge for optimization and control," *at-automatisierungstechnik*, vol. 57, no. 10, pp. 525–533, Jul. 2009.

[8] B. Houska and M. Diehl, "Optimal control for power generating kites," in *Proc. 9th European Control Conference ECC '07*, Kos, Greece, Jul. 2–5, 2007, pp. 3560–3567.

[9] Joby Energy. Accessed: April 2011. [Online]. Available: http://www.jobyenergy.com

[10] Sky WindPower. Accessed: April 2011. [Online]. Available: http://www.skywindpower.com

[11] Makani Power. Accessed: April 2011. [Online]. Available: http://www.makanipower.com

[12] J. Sun, "Small-signal methods for ac distributed power systems–a review," *IEEE Trans. Power Electron.*, vol. 24, no. 11, pp. 2545–2554, Nov. 2009.

[13] D. Boroyevich, I. Cvetković, D. Dong, R. Burgos, F. Wang, and F. Lee, "Future electronic power distribution systems – a contemplative view," in *Proc. 12th International Conference on Optimization of Electrical and Electronic Equipment OPTIM '10*, Brasov, Romania, May 20–22, 2010, pp. 1369–1380.

[14] J. W. Kolar, J. Biela, and J. Miniböck, "Exploring the pareto front of multi-objective single-phase PFC rectifier design optimization – 99.2% efficiency vs. $7\,kW/dm^3$ power density," in *Proc. 6th IEEE International Power Electronics and Motion Conference IPEMC '09*, Wuhan, China, May 17–20, 2009, pp. 1–21.

[15] J. W. Kolar, J. Biela, S. Waffler, T. Friedli, and U. Badstübner, "Performance trends and limitations of power electronic systems," in *Proc. 6th International Conference on Integrated Power Electronics Systems CIPS '10*, Nuremberg, Germany, Mar. 16–18, 2010, pp. 1–20.

[16] Cortland Cable. Accessed: April 2011. [Online]. Available: http://www.cortlandcable.com

[17] E. Murtola, S. M. Neuhold, and P. Anliker, "Hyperelastic high voltage conductor for electric drilling," in *Proc. 4th International Conference on Composite Materials & Structures for Offshore Operations CMOO '05*, Houston (TX), USA, Oct. 4–6, 2005, pp. 1–11.

[18] S. M. Neuhold, "A hyper elastic conductor for bulk energy transfer in the wall of spoolable tubes for electric deep drilling," Ph.D. dissertation, Swiss Federal Institute of Technology Zurich (ETH Zürich), 2007.

[19] Huber+Suhner, "Radox GKW Cables," datasheet, 2011.

[20] Klotz a+i+s, "AWG Tabelle," data table, 2005.

[21] P. Ragot, M. Markovic, and Y. Perriard, "Optimization of electric motor for a solar airplane application," *IEEE Trans. Ind. Appl.*, vol. 42, no. 4, pp. 1053–1061, July/Aug. 2006.

[22] J. Cros and P. Viarouge, "Synthesis of high performance PM motors with concentrated windings," *IEEE Trans. Energy Convers.*, vol. 17, no. 2, pp. 248–253, Jun. 2002.

[23] M. Schweizer, I. Lizama, T. Friedli, and J. W. Kolar, "Comparison of the chip area usage of 2-level and 3-level voltage source converter topologies," in *Proc. 36th IEEE Industrial Electronics Conference IECON '10*, 2010, pp. 391–396.

[24] T. Friedli and J. W. Kolar, "Comprehensive comparison of three-phase ac–ac matrix converter and voltage dc-link back-to-back converter systems," in *Proc. IEEE/IEEJ International Power Electronics Conference -ECCE Asia- IPEC '10*, Sapporo, Japan, Jun. 21–24, 2010, pp. 2789–2798.

[25] ——, "A semiconductor area based assessment of ac motor drive converter topologies," in *Proc. 24th IEEE Applied Power Electronics Conference and Exposition APEC '09*, Washington DC, USA, Feb. 15–19, 2009, pp. 336–342.

[26] U. Drofenik, G. Laimer, and J. W. Kolar, "Theoretical converter power density limits for forced convection cooling," in *Proc. 26th European Power Electronics/Intelligent Motion/Power Quality Conference PCIM '05*, Nuremberg, Germany, Jun. 7–9, 2005, pp. 1–12.

[27] M. H. Kheraluwala, R. W. Gascoigne, D. M. Divan, and E. D. Baumann, "Performance characterization of a high-power dual active bridge dc-to-dc converter," *IEEE Trans. Ind. Appl.*, vol. 28, no. 6, pp. 1294–1301, Nov./Dec. 1992.

[28] F. Krismer, "Modeling and optimization of bidirectional dual active bridge dc–dc converter topologies," Ph.D. dissertation, Swiss Federal Institute of Technology Zurich (ETH Zürich), 2010.

[29] F. Krismer and J. W. Kolar, "Efficiency-optimized high current dual active bridge converter for automotive applications," *IEEE Trans. Ind. Electron.*, pp. 1–16, 2011, accepted for future publication.

[30] ——, "Accurate power loss model derivation of a high-current dual active bridge converter for an automotive application," *IEEE Trans. Ind. Electron.*, vol. 57, no. 3, pp. 881–891, March 2010.

[31] F. W. Lanchester, "A contribution to the theory of propulsion and the screw propeller," *Trans. of the Inst. of Naval Architects*, vol. LVII, pp. 98–116, 1915.

[32] A. J. Healey, S. M. Rock, S. Cody, D. Miles, and J. P. Brown, "Toward an improved understanding of thruster dynamics for underwater vehicles," *IEEE J. Ocean. Eng.*, vol. 20, no. 4, pp. 354–361, Oct. 1995.

[33] G. G. Carlos, "Design of a 3.5 meters rotor two bladed horizontal axis wind turbine," in *Proc. 20th International Conference on Electronics, Communications and Computer CONIELECOMP '10*, Puebla, Mexico, Feb. 23–24, 2010, pp. 247–251.